PRECISION ENGINEERING CENTER

2007 INTERIM REPORT
September 2007

Sponsors:

3M Corporation
BWX Technologies
Lexmark International, Inc.
National Science Foundation
Optical Research Associates
Panasonic Technologies, Inc.
United States Department of Energy
Vistakon, Johnson & Johnson Vision Care Inc.

Faculty:

Thomas Dow, Editor
Greg Buckner
Jeffrey Eischen
Paul Ro
Ronald Scattergood
David Youden

Graduate Students:

Qunyi Chen
David Brehl
Karalyn Folkert
Timothy Kennedy
D. Lucas Lamonds
Jorge Esguerra
Stephen Furst
Yanbo Yin

Staff:

Kenneth Garrard
Karl Falter
Wendy Shearon
Donna Irwin
Alexander Sohn

TABLE OF CONTENTS

1 FRESNEL LENS DESIGN SOFTWARE

Kenneth Garrard
Precision Engineering Center Staff

1.1 INTRODUCTION

Fresnel lenses have typically been used for non-imaging applications, primarily because of the undesirable effects of groove structure on image quality. For this reason, optical design software for imaging applications generally only addresses Fresnel lenses in a very simplified manner. For example Zemax, Code V and Oslo treat Fresnel surfaces as ideal thin lenses with a surface curvature function to give the lens power[1]. This thin lens may be flat or superimposed on a curved substrate, which also provides power. In particular, the design codes do not consider the groove structure or manufacturing artifacts of Fresnel lenses. While this approach is adequate for many applications, it appears to lack attention to the item of most concern in the design of Fresnel lenses for laser scanning systems: The influence of the groove structures. For this reason a more direct design and modeling approach has been taken and tailor-made optical design software is being developed. Recent progress in the development of this software is described below.

Fresnel lenses can provide optical power without the bulk of a conventional lens. Figure 1 shows how a plano-convex lens is collapsed into a Fresnel lens to provide a thinner lens with similar optical properties. Thinner lenses are easier and less expensive to replicate via molding than thick lenses or lenses with a large thickness variation. A thinner lens can also be expected to absorb less light. Diffraction from the structure at each zone boundary and its influence on the focusing characteristics of the lens and transmission efficiency are discussed in Section 2.

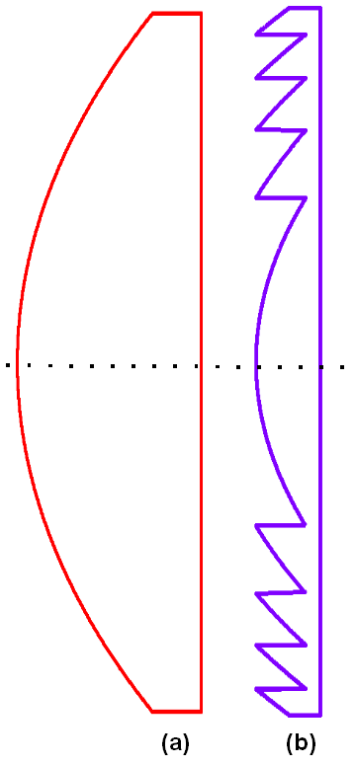

Figure 1. A conventional lens (a) is collapsed to form a Fresnel lens (b).

[1] Non-sequential ray trace software such as TracePro and Zemax EE can analyze arbitrary surfaces but do not support their design or optimization.

1.2 ASPHERIC FRESNEL LENS DESIGN

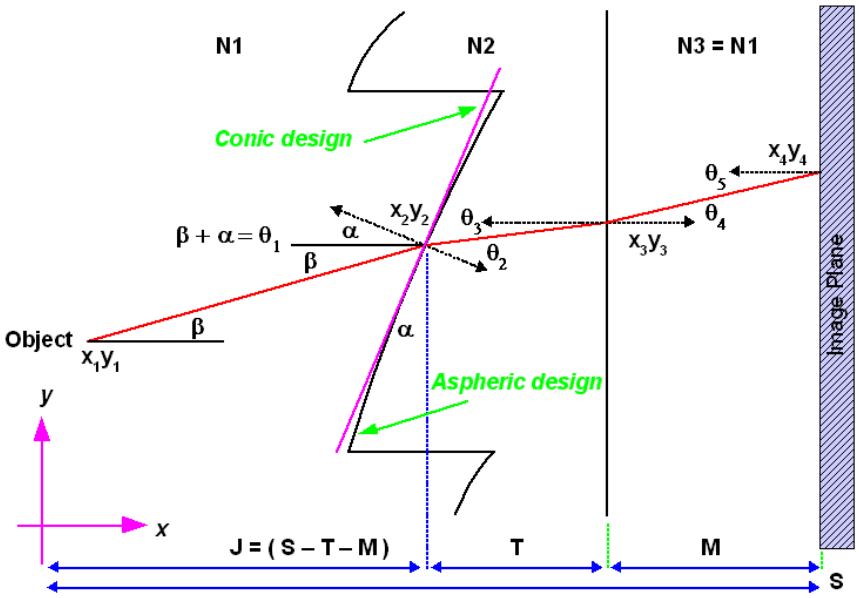

Figure 2. Ray propagation through a single Fresnel lens zone. For a conic design the surface slope for the central ray shown in red is used for an entire zone, whereas for an aspheric design, the slope changes continuously through the zone to focus each ray onto the image plane.

Ray propagation through a single lens is shown in Figure 2 for both a conic (i.e., flat) and an aspheric Fresnel lens zone. The equations describing the relationship between the ray heights and refraction angles are given in [1,2]. The conical Fresnel lens design code produces a lens with constant zone width and varying depth. Only one ray at the center of each zone is used to find the slope for that zone (as shown in magenta in Figure 2). That ray exactly intersects the focal plane at the desired ray height; however other rays in that zone intersect the focal plane above or below the focal point. By reducing the ray height spacing more conical zones (i.e., prisms) are produced and more rays arrive at the correct location on the focal plane. But there are disadvantages to increasing the number of zones. A larger percentage of the lens surface is either shadowed or does not direct incoming light toward the focal plane (e.g., rays incident on trough radii). For a scanned beam, as the beam angle increases the amount of light that enters the lens on the vertical zone boundaries increase. Also with increasing radius the slope of each prism is steeper and since zone width is constant the depth must increase. Thus the zone step height increases. Machining a conical Fresnel surface with many zones requires a small radius or dead-sharp tool which is fragile. The time to achieve an acceptable surface finish may be very long and tool wear and process stability will limit performance.

An alternative to conical Fresnel zones with constant slope is to vary the slope with radius so that all incident rays converge at the desired focal point. For example, in Figure 1 the curvature of the

plano-convex lens (a) is replicated in each zone of the collapsed Fresnel lens (b). Since the surface of each zone is translated along the optical path and the lens is thinner, the curvature of each zone must change to maintain focus. An analytic formulation of how the curvature changes as a result of the collapsing process with respect to the optical characteristics of the lens (i.e., incoming and outgoing wavefront) is being studied.

1.2.1 ITERATIVE LENS DESIGN

A numeric algorithm for iteratively designing an aspheric Fresnel lens has been developed [1]. Coded in Matlab, this algorithm finds the required surface slope for each ray in a one element optical system. It does not optimize the slope for multiple rays with different object and image requirements, i.e., the beam scanning problem. Instead each ray is considered independently and by iterating from the inside (optical axis) to the outside (maximum radius) a lens shape is found that focuses each ray to an image point. The intersection of each incoming ray with the extension of the surface from the previous iteration is found. Then a new slope is calculated for this point that satisfies the focal criteria and the process co ntinues. By considering a large number of closely spaced parallel rays, an approximation to the continuous surface that perfectly focuses the light is built point-by-point. Without constraining the x or y location of points on the lens surface a general plano-convex aspheric lens is produced. For a Fresnel lens, displacement parallel to the optical axis (x direction) is limited to a fixed amount and a step in the negative direction (back toward the object) is taken when this limit is exceeded as shown in Figure 3. The result is a Fresnel lens with constant zone depth, arbitrary zone width and curved zone profiles. Figure 4 shows the profile of a 200 mm focal length Fresnel lens (object at infinity) with 100 mm aperture that was designed by this code. The lens is 2.33 mm thick (top of zone steps to lens back). As expected, the constant depth zone profiles become narrower and steeper with increasing radius.

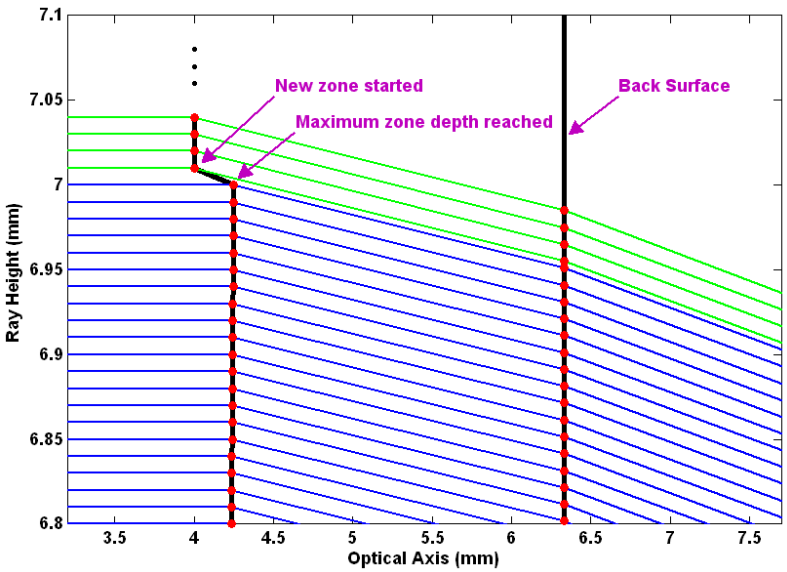

Figure 3. Aspheric lens design process. When the maximum zone depth is reached (blue), a new zone is started (green).

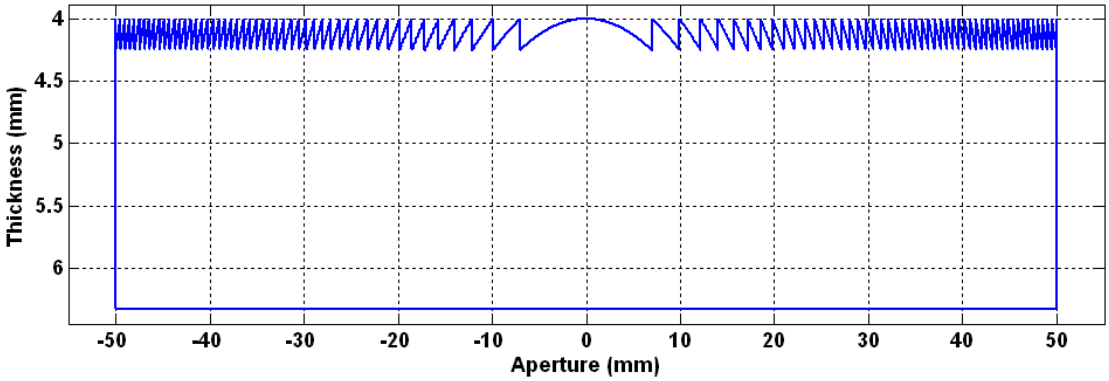

Figure 4. F200 Aspheric Fresnel lens with 51 zones. (The aspect ratio of the plot is not 1:1).

Each iteration of the design code depends on the prior ray trace results only in that those rays were used to arrive at the local slope of the current ray-surface intersection point. Thus the constraints: incoming rays parallel and normal to the lens, focus at a single point on the image plane, constant zone depth, unrestricted zone width and plano back surface are not limitations of the algorithm. As long as the only unknown parameter for each ray is the front lens surface slope a unique solution can be found by a nonlinear root finding procedure [2]. The principle difficulty with varying the zone depth and width or having a curved lens back surface is determining the criteria for changing those parameters.

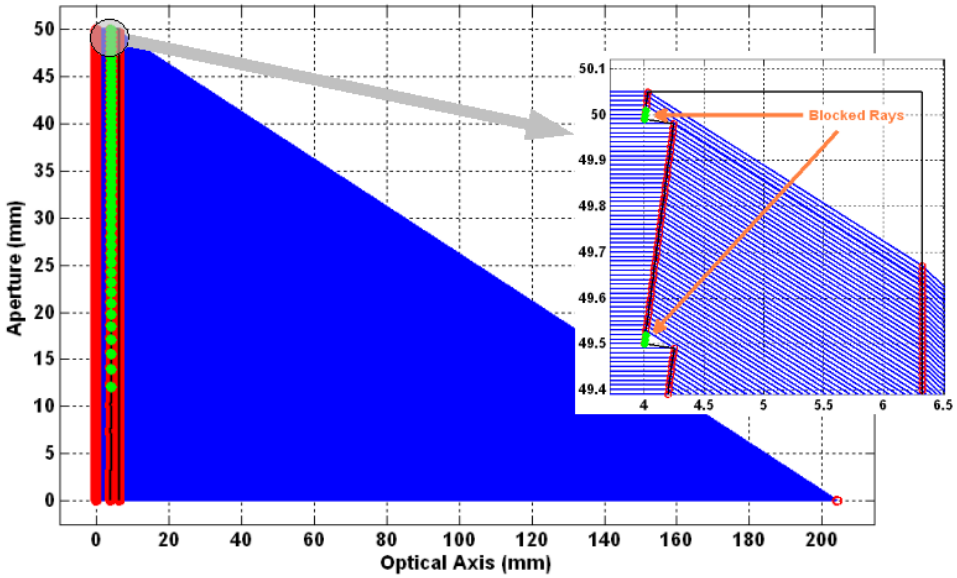

Figure 5. Complete aspheric lens design with blocked rays indicated by green dots.

Figure 5 shows a completed aspheric design ray trace with intersection points marked by red circles and blocked rays indicated by green dots. A ray is blocked when it is refracted at the front surface of the lens so that it does not intersect the back of the lens. As seen in Figure 5 this

happens at the start of a new zone when the surface slope is steep enough to cause the refracted ray to strike the inside of the prior zone step. More rays are blocked if the zones are deeper or the aspheric surface curvature increases. For this lens, about 2.8% of a normal incidence, parallel wavefront is blocked.

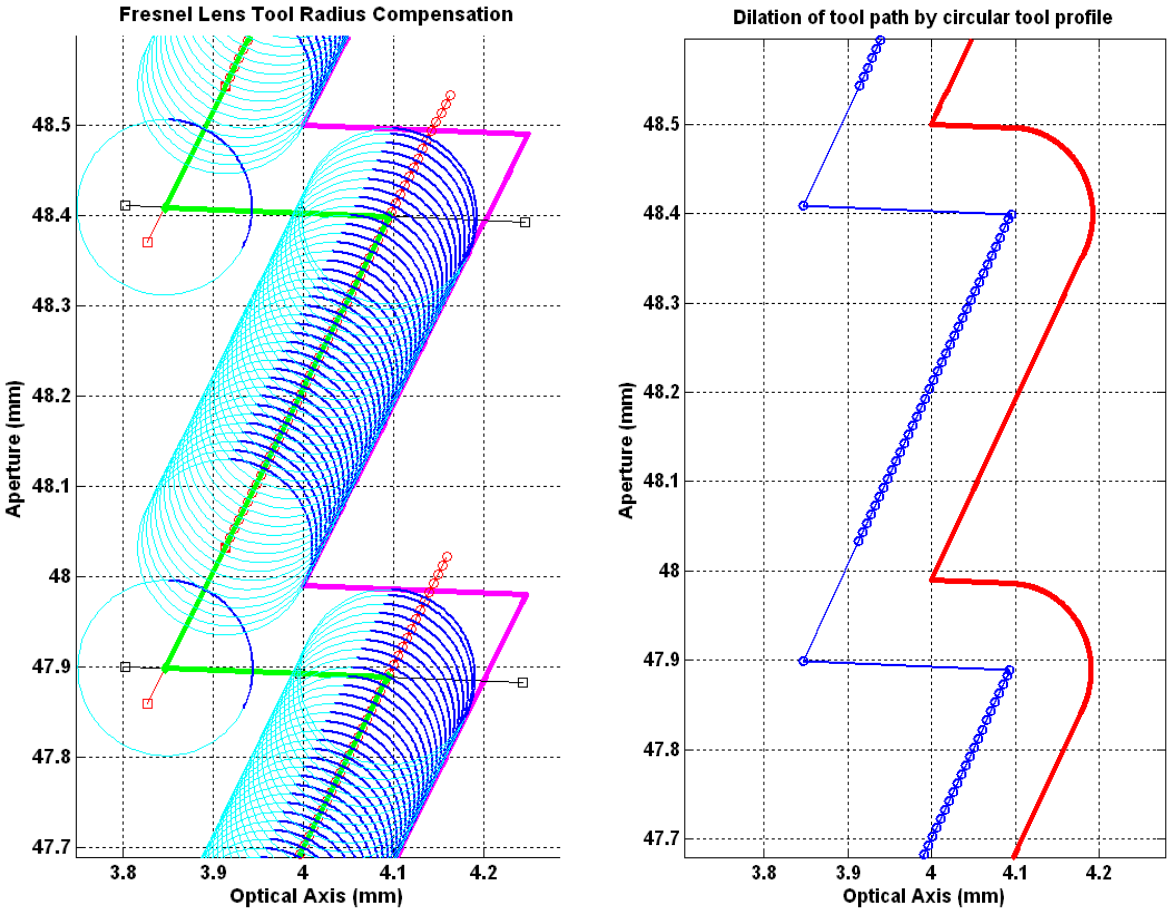

(a) (b)

Figure 6. Tool radius compensation for a Fresnel lens. In (a) the magenta line is the aspheric Fresnel lens, the green line is the tool path and the blue arcs are successive tool edge positions. In (b) the blue line with dots is the path followed by the center of the tool and the solid red line is the resulting machined surface with a radius at the bottom of each zone transition.

1.2.2 TOOLING ARTIFACTS

It is apparent from Figure 4 that the shape of the front surface of this Fresnel lens cannot be machined with a convex tool. The bottom of each zone is the concave intersection of a straight line (zone step) and a convex curve and thus has no curvature. A close approximation to the surface can be machined with a small radius tool at the expense of long cutting time to achieve acceptable surface finish. For a circular tool profile in the xy plane, the path of the tool center

that results in the tool edge tracing out the desired surface shape must be calculated. For a continuous surface this is a straightforward process, but for a Fresnel lens the zone intersections must be handled as a special case. At each zone boundary the tool must be tangent to both the aspheric profile and the nearly vertical, flat wall of the zone step. However as shown in Figure 6a the tool cannot cut one surface completely without over-cutting the other surface at the concave intersections. The intersection of normal vectors from each surface with length equal to the tool radius identifies this transition point. The convex intersection can be achieved with a radius tool. The transition point is the intersection of the two tool paths after extending each along the same slope as its endpoint. Matlab code that finds these intersections and generates a motion program for the PEC's custom controller for the ASG 2500 Diamond Turning Machine has been written.

The intersection of each zone asphere with the zone step will resemble the shape of the tool as the transition is made in the cutting path from negative slope to positive slope at the bottom of each zone. Figure 6b shows a plot of the surface that would be machined by the cutting path generated by Fresnel tool radius compensation code discussed above. This process is equivalent to the morphological dilation of the tool path (an image) with the projection of the tool into the cutting plane (a structuring element).

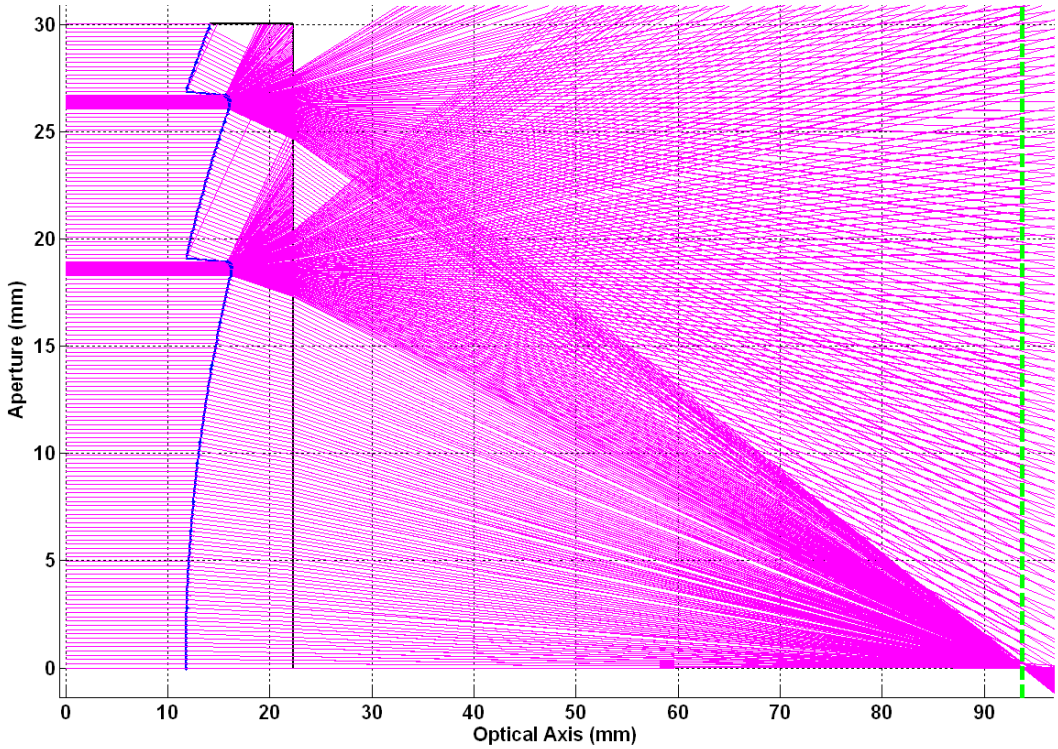

Figure 7. Raytrace through a Fresnel lens. The diverging rays from the tooling arcs flood the image plane from about 1 mm above the focal point to infinity. Some of these rays internally reflect at the back surface. The rays through the aspheric zones converge at the focal point.

A procedure to trace rays through the as-fabricated lens shape was written to 1) validate the process of creating the tool path from the design (i.e., Do parallel rays converge at the focal point?) and 2) investigate the effects of the diverging rays incident on the concave arcs left by the tool at the zone boundaries. This code is given in [1] and can also be used to simulate the effect of thickness variation on focus, tilt in the incoming wavefront and numerous other geometric variations. Figure 7 shows the ray trace results for an 80 mm focal length Fresnel lens. Note that the ray fans diverge from the concave tooling arc corners and cover the image plane. None of these rays converge to the focal point, but they do represent a loss of efficiency. However some light incident at the top of the convex zone transitions that would be blocked by perfect trough intersections at the bottom of each zone makes it through the lens because the trough is truncated into a rounded corner.

1.3 CONCLUSIONS AND FUTURE WORK

An iterative aspheric zone Fresnel lens design code has been developed. The code includes toolpath generation and ray tracing through a simulated as-machined surface. Additional code to support the ray trace operations is given in the appendices to [1] and includes a vector solution to Snell's law in 3D and a general purpose, robust 2D curve intersection routine. Extension of the ray trace code to arbitrary 2D input shapes is current being implemented. Future work includes a 3D implementation of the aspheric design code that optimizes surface curvature to focus a scanning laser beam.

REFERENCES

1. Dow, T., K. Garrard and A. Sohn. Final Report – Phase I, Fresnel Scanning Lens Design. Precision Engineering Center, North Carolina State University (2007).
2. Sohn, A., K. Garrard and T. Dow. Fresnel Lenses for Scanning Systems. Precision Engineering Center Annual Report, 24, 229-248, (2006).

2 FAST LONG RANGE ACTUATOR (FLORA)

Qunyi Chen
Graduate Student
Thomas A. Dow and Gregory Buckner
Professors, Mechanical and Aerospace Engineering
Kenneth Garrard and Alex Sohn
PEC Staff Member

2.1. BACKGROUND

Diamond turning (DT) has revolutionized the fabrication of optical surfaces for consumer, defense and science applications such as contact lenses, forward-looking infrared radar and infrared spectrometers. It has made this impact not only because it can accurately and rapidly fabricate diffractive, refractive and reflective optical surfaces, but also because it can create reference features tied to the optical surfaces to assist in the assembly process. An emerging trend in optical design is the use of Non-Rotational Symmetric (NRS) surfaces to reduce complexity, bulk and weight while improving optical performance. To create these so-called freeform surfaces, DT machines have been operated at very slow spindle speeds or modified with a piezoelectric Fast Tool Servo (FTS) or a flycutter. The proposed Long Range Actuator (FLORA) integrates existing technologies (air bearings, linear motors, high-resolution encoders and real-time control) into a lightweight, moving tool holder that can be retrofitted onto a conventional DT machine.

The goal of the FLORA is to create optical quality surfaces while moving the tool over a range of ± 2 mm at a frequency of 20 Hz. The technical challenges include:

Form Error Diamond turning machines can create excellent form fidelity because of their stiff, linear slides and air-bearing spindles. Reducing the moving mass will improve the bandwidth of the system but also make it more susceptible to disturbances.

Surface Finish Simple theoretical relationships between machining parameters (spindle speed, axis velocity) and tool geometry can be used to predict surface finish. However, the dynamic conditions envisioned for the FLORA may play a more significant role.

2.2. SYSTEM DEVELOPMENT

A prototype FLORA was built during 2004 and has continued with support from NSF. The FLORA has a light-weight honeycomb triangular piston, a linear motor and a high-resolution

linear encoder. The total range of motion of the motor is 50 mm but the goal is a stroke of 4 mm at 20 Hz. A photograph of the actuator is shown in Figure 1.

To improve the surface finish and figure error for this actuator, a number of changes to the electronic components were made over the past 6 months.

- High-resolution encoder – A Sony glass scale encoder was added to provide piston position feedback with 0.25 nm resolution at speeds up to 750 mm/sec.
- Linear Amplifier – An Aerotech linear amplifier BL10-80A is being used to drive the Airex linear motor. The amplifier has a maximum current output of ±10 Amps with a bandwidth of 2000 Hz. The motor can produce a peak force of 81 N.
- Control platform – A PMDi controller has been installed that can provide an update time of 25 µsec or 40 Kz. This system uses an Analog Devices SHARC processor 40 MHz ADSP-21061L.

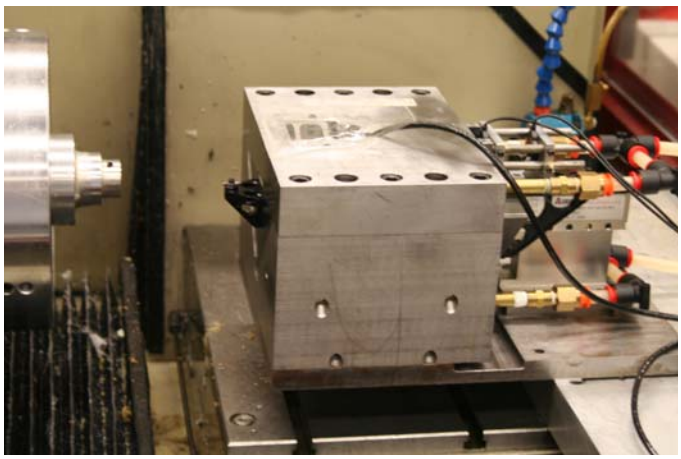

Figure 1. Photograph of the FLORA system mounted on the ASG 2500 DTM.

2.3. OPEN LOOP TRANSFER FUNCTION

The single DOF system shown in Figure 1 consists of moving piston in an air bearing (an undamped mass m), the actuating force $K_f I$ from the linear motor and the tool feeding position $z(t)$ from the linear encoder. Figure 2(a) shows the measured open loop system transfer function for position output in mm to input in current to the amplifier. Figure 2(b) shows the result the command amplitude is modified based on Equation (1) to remain at the same level. In this case the transfer function is from mm command to mm motion

$$A = \frac{K_f I}{m\omega^2} \tag{1}$$

The peak in Figure 2(b) at 900 Hz is due to the analog current loop within the amplifier and motor. Additional resonance peaks above 1000 Hz are due to aerodynamic effects in the linear air-bearing. The existence of these high frequency dynamics limits the capability of conventional feedback controller design.

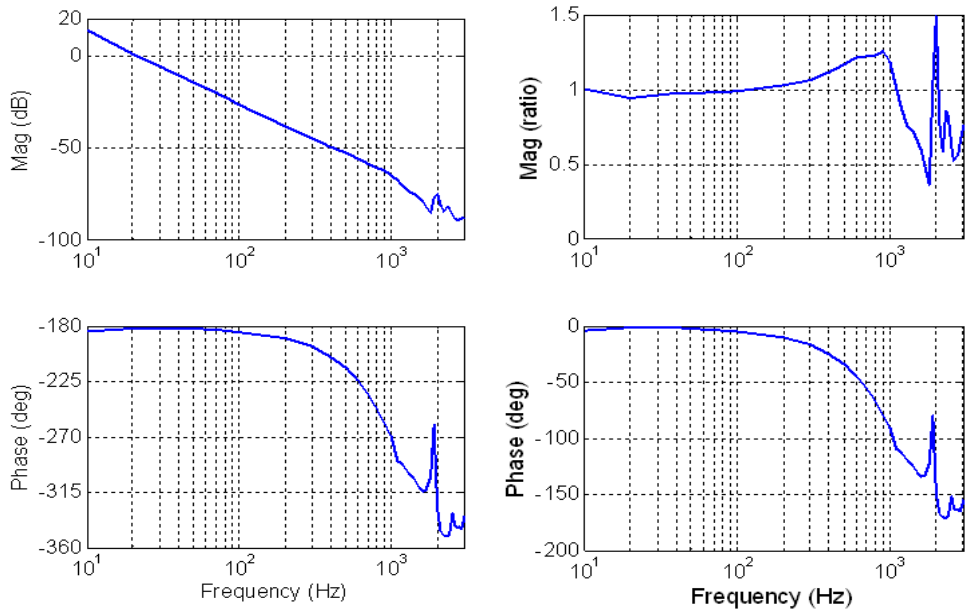

(a) (b)

Figure 2. Commutated open loop system transfer function frequency responses from current command (a) and corrected for system inertia (b) using Equation (1)

2.4. CONTROL SYSTEM DESIGN

The controller design is based on the measured open loop frequency response and desired closed-loop system performance specification. A PID controller (Equation (2)) was first designed due to its intuitive nature and the gains are determined by trial-and-error tuning process. A frequency design approach using a lag-lead controller was followed to obtain desired frequency response across all frequency range and the result is Equation (3). The frequency response of the closed-loop system transfer function resulted from each controller is shown in Figure 3(a).

$$K_{PID}(z) = \frac{3321.1z^2 - 6518.9z + 3200}{z^2 - z} \quad (2) \qquad K_{LL2}(z) = \frac{4355z^3 - 11928z^2 + 10878z - 3303}{2z^3 - 4.4197z^2 + 3.1516z - 0.73186} \quad (3)$$

These two controllers behave similarly in the frequency domain; that is, they increase loop gains at low frequency, add phase lead to obtain phase margin at the crossover frequency and lower the gain at high frequency. A comparison of the theoretical closed-loop system frequency response is shown in Figure 3. The transfer function in Figure 3(a) is from position command to the output position. It shows the closed-loop system has a bandwidth of 1122 Hz with the PID controller and 1594 Hz with the lag-lead controller. As a result, the closed-loop response for the lag-lead will be faster but with slightly larger overshoot. The sensitivity function in Figure 3(b) is a measure of the error in tracking commands at low frequency and rejecting disturbances at high

frequencies. The position error is (1-1/magnitude) in this graph and it shows results that would not be visible in Figure 3(a) especially at low frequency. For a sine wave command using the PID controller at 20 Hz, the magnitude is -52 dB, the error is 0.25% and the amplitude ratio is 0.9975. This is close to one as shown in Figure 3(a).

It is important to make the sensitivity magnitude small and Figure 3(b) shows the typical tradeoffs involved in feedback control design.

1. The lag-lead controller will minimize tracking errors and disturbance forces at frequencies lower than 1000 Hz. Below 100 Hz, the sensitivity magnitude from the lag-lead controller is about half that of the PID controller. This simulation result has been verified by the experiments with a disturbance at 60 Hz.
2. Both controllers have nearly the same peak sensitivity magnitude but the lag-lead controller peaks at a higher frequency (1200 Hz) than the PID (800 Hz). This behavior will amplify disturbances above 1000 Hz.

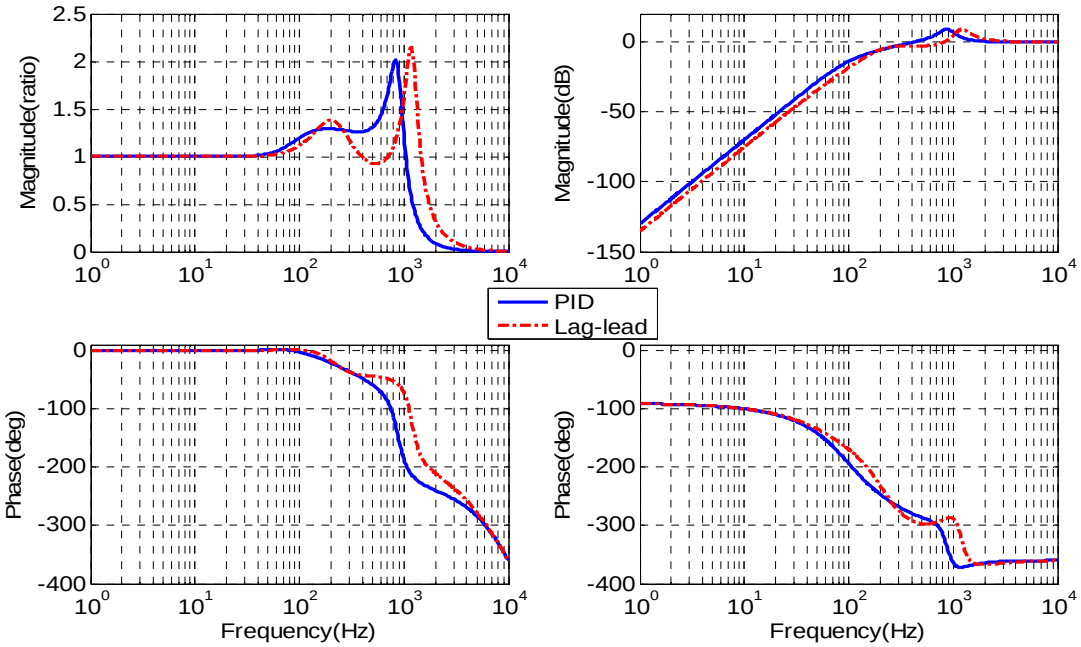

(a) Transfer function (b) Sensitivity function

Figure 3. Closed loop simulations for PID and Lag-lead controllers

The design process involves a compromise between reducing low frequency error magnitude and improving disturbance rejection at high frequency as shown in Figure 3(b). Figure 4 shows the frequency spectrum of the piston motion when holding position. Error for the PID controller is ±40 nm PP (10.8 nm RMS) and ±30 nm PP (8.0 nm RMS) for the Lag-lead. It is clear that the amplitudes are much smaller for frequencies less than 1000 Hz in the case of lag-lead controller.

With these two controllers design, additional studies on sensitivity function have been performed regarding the need for physical damping and most desirable piston mass.

1) Physical damping is not needed for the FLORA. At high frequencies the amplitudes and thus the forces are too small to make any appreciable difference. At low frequency and high amplitude, the damping forces are high but are not needed and only lead to higher motor force.
2) When the closed-loop system sensitivity magnitude frequency response exceeds 0 dB, the system relies totally on the mass to reject disturbances and noise. The controller actually amplifies the disturbances at frequencies higher than crossover frequency (430 Hz for the PID controller, 830 Hz for the lag-lead controller in Figure 3(b)). As a result of the high frequency disturbance with current FLORA design and achievable controller design, a smaller piston mass will reduce the system disturbance rejection capability.

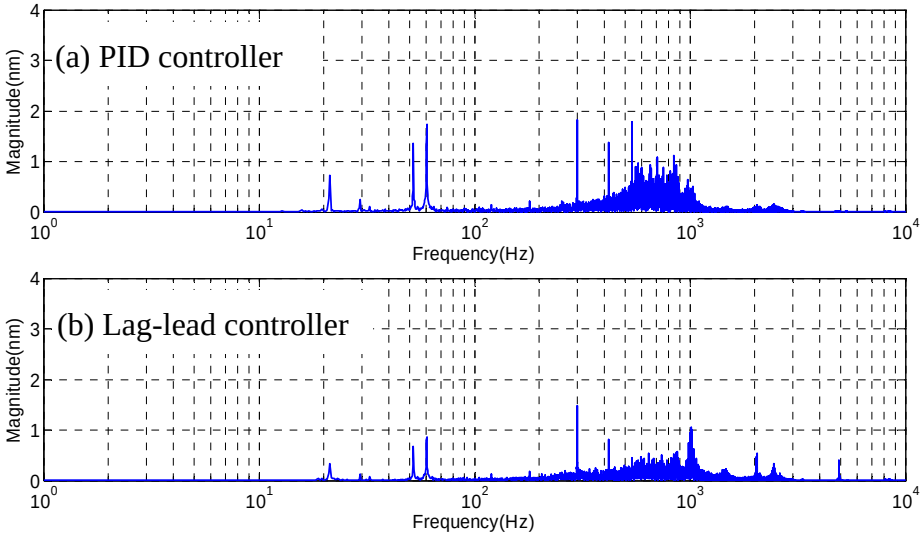

Figure 4. Frequency spectrum of position data when holding position

2.5. CUTTING PERFORMANCE

A flat surface was machined to test the ability of the FLORA piston to hold position while excited by the forces of machining. Figure 1 shows the FLORA mounted on the ASG-2500 DTM. The flat was machined with a 0.5 mm radius diamond tool at 500 rpm with a 2 mm/min feedrate (4 μm/rev) and 2 μm depth of cut on the finish pass. The theoretical finish is 4 nm PP. The Zygo NewView measurement in Figure 5 shows a 144×108 μm patch represents approximately 72 tool passes and has an average surface finish of 9.0 nm (RMS).

Table 1 compares the motion of the piston and the RMS finish of flat surface when the tool is locked or held in positioned by the control system. For the locked case, the air pressure was

removing from the lower sides of the triangular piston but retaining the preload pressure. This is the same surface finish achieved under these conditions using a standard tool holder. Table 1 shows the piston motion as measured by the encoder. For the locked tool there is little piston motion but when the air bearing is turned on and the motor is used hold the piston, the motion is increased to 8 nm RMS for the Lag-lead controller and 13.1 nm for the PID. The surface finish is also increased when the piston is unlocked. The active closed-loop control using the Lag-lead algorithm adds 2.3 nm RMS to the surface finish and the PID adds 5.6 nm.

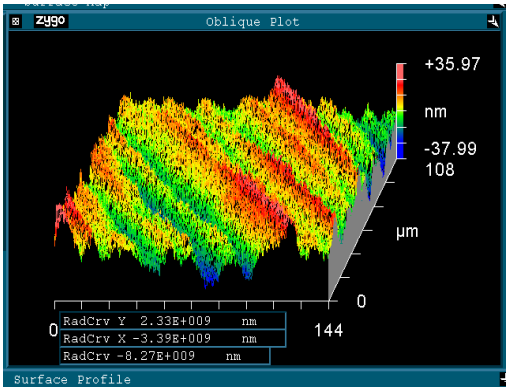

Figure 5. ZYGO image of surface finish (RMS=9 nm) on a plated copper flat.

2.6. CONCLUSIONS

The FLORA control system has been upgraded with a high-resolution encoder, a linear amplifier and a high-speed DSP based controller. The key conclusions are as follows:

1. High controller gain in the frequency range below 1000 Hz is needed to reduce tracking error at 20 Hz and reject cutting force disturbance at the natural frequency of the z slide of the DTM which is approximately 60 Hz. Improved performance could be achieved if the high frequency (>1000 Hz) dynamics within the FLORA can be minimized physically.
2. The feedback control design approach achieved reasonable performance over the range of frequencies of interest. It will be combined with feed-forward control and other more advanced control approaches to improve the tool positioning performance.
3. The system changes discussed in this paper improved the position holding capability by 85% over the system described in 2006 [1].

Table 1. Comparison of RMS error with a locked and position controlled tool holder

	Tool holding method		
	Piston Locked	**Lag-lead controller**	**PID controller**
Piston Motion, nm RMS	1	8.0	13.1
Surface finish, nm RMS	6.7	9.0	12.3

2.7. ACKNOWLEGEMENT

Principal funding for this work is by National Science Foundation grant DMI-0556209, monitored by G. Hazelrigg. PMDi has provided valuable assistance with the control system development.

3 ULTRAMILL COOLING SYSTEM

David Brehl
Graduate Student
T. A. Dow
Professor

3.1. BACKGROUND

The Ultramill, an Elliptical Vibration-Assisted Machining (EVAM) tool, is driven by piezoelectric actuators which produce waste heat as a result of hysteresis during their expansion/contraction cycle. The heat generation in the Ultramill is sufficiently large that the actuators need to be actively cooled, to achieve a safe operating temperature below 100 C. Figure 1-1 depicts the Ultramill thermal control system. Heat is removed from the piezoelectric stacks (1) by continuously circulating dielectric coolant (2). Pressure to move the coolant through the system is created by a diaphragm pump (3) in the Thermocube temperature control unit. The Thermocube contains a solid-state thermoelectric heat exchanger (4) that adds or removes heat as required to keep the coolant at a programmed setpoint temperature. Its internal temperature sensor (5) measures the temperature of the coolant returning from the Ultramill, compares it to the setpoint and uses the cooler/heater to drive it to zero.

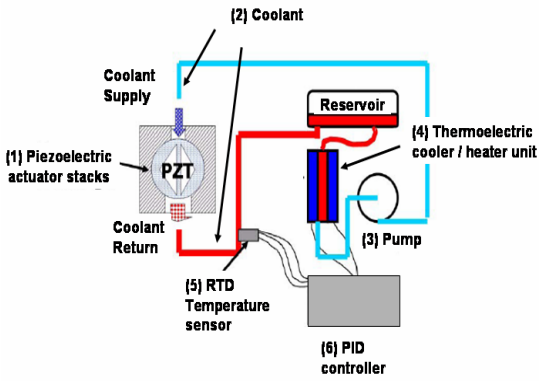

Figure 1. Diagram of Ultramill Thermal Control System

Because the Thermocube uses a positive-displacement pump, there was concern that connecting the coolant supply line directly to the Ultramill would cause its structure to vibrate due to pump induced pressure pulsations, which in turn would cause error in machined surfaces. Therefore from its initial installation until May 2007, the Ultramill used an open-circulation cooling scheme. In April 2007 an investigation of closed circulation cooling was initiated to compare the quality of the surfaces produced. The goal of these investigations was to:

1. Reduce the temperature of the Ultramill by increasing the effectiveness of the heat transfer process,
2. Improve the temporal stability of the Ultramill temperature and
3. Isolate the Ultramill from the vibration induced by the diaphragm pump.

3.2. SYSTEM CONFIGURATIONS

Figure 2 shows the original open-circulation configuration of the Ultramill cooling system and the closed-circulation configuration that were investigated.

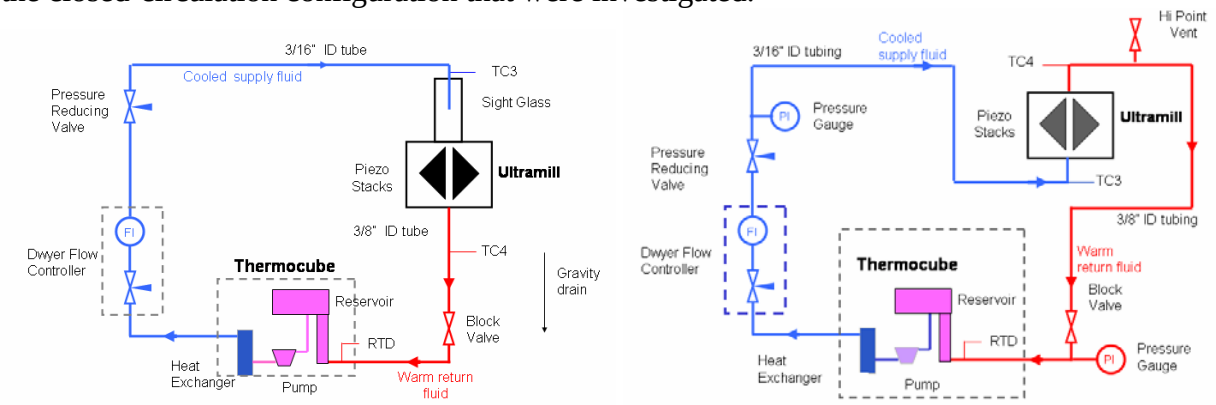

Figure 2. Open-circulation cooling arrangement (left) and closed-circulation (right)

In the open-circulation arrangement, the coolant was supplied from the Thermocube by the diaphragm pump. During steady-state operation, the coolant leaving the Thermocube was cooled below the setpoint (return) temperature at inlet to the Thermocube and increased in temperature as it passed over the actuator stacks. The volumetric flow rate was adjusted using a rotameter-type flow controller. A pressure reducing valve, downstream of the flow controller, was used to improve the resolution of the flow controller by taking up most of the pressure difference between ambient and the pressure provided by the diaphragm pump. The coolant discharged into a sight glass mounted above the Ultramill cooling chamber. It then flowed by gravity into the coolant return line. Since the liquid level in the sight glass is only 80 mm above the centerline of the cooling chamber, the liquid pressure at the preload diaphragm-toolholder interface is 1.5 KPa (0.2 psi). At this low pressure, little if any fluid leaks from the coolant chamber. To facilitate gravity-driven flow, the Thermocube was located on the floor, about 1.2 m below the center line of the Ultramill.

Figure 2 also shows the closed-circulation cooling arrangement with the coolant supply line connected to the bottom port of the Ultramill cooling chamber. The volumetric flow rate of the coolant is still controlled by the rotameter-type flow controller with the pressure reducing valve. The coolant return connection is on the top of the Ultramill. The coolant return line contains a high-point vent which is used to evacuate air from the system when it is first filled with fluid. In the closed-circulation configuration, the Thermocube is located above the Ultramill to help any air bubbles in the coolant circuit flow away from the Ultramill. In closed-circulation cooling, the pressure in the Ultramill cooling chamber is 30 to 150 KPa (5 – 15 psi) above atmosphere. This

high pressure causes some coolant leakage from the joint between the toolholder and preload diaphragm.

3.3. EXPERIMENTAL RESULTS

Three types of experiments were conducted to evaluate the differences between the open and closed coolant circulation schemes.

1. Temperature measurements from thermocouples placed throughout the coolant path
2. Surface finish results from machining experiments
3. Capacitance gage measurements of the tool location as a function of time

3.3.1. TEMPERATURE MEASUREMENTS

Figures 3 shows the temperature data recorded during Ultramill operation driven with 400 V_{PP} at 1 KHz. Figure 3(a) shows data for the gravity-driven open-circulation configuration. The coolant flow rate varied between 0.30 and 0.40 L / min as adjustments were made to keep a constant liquid level in the sight glass. Figure 3(b) shows temperature data for the closed-circulation configuration with coolant flow maintained at approximately 0.4 L/min.

The top plot shows the temperature measured by thermocouple on inside face of the actuator stack. The bottom plot shows the temperature of coolant at inlet and outlet of Ultramill cooling chamber. With open-circulation cooling the indicated stack temperature is seen to fluctuate across a range of several degrees, with abrupt changes observed. In contrast, the stack temperature plot for closed-circulation cooling is nearly constant. It is also at a lower temperature indicative of higher heat convection heat transfer coefficient between the stack surfaces and the circulating coolant. The inset in the top panel of Figure 3(b) shows a portion of the stack temperature plot at the same time scale but at a finer temperature resolution. It is seen that the indicated stack temperature actually fluctuates cyclically with a period of approximately 3.3 minutes and a 0.4˚C peak-to-peak magnitude. The bottom panel in each figure plots the temperatures of the coolant stream entering and leaving the Ultramill. In the closed circulation case in Figure 4, the coolant temperatures cycles practically in phase with the stack temperature, again with a period of about 3.3 minutes. This period is believed to reflect the natural frequency for the installed cooling system arrangement (i.e. the length and volume of the coolant hoses, Ultramill volume, and Thermocube heat rejection capability have a fundamental response characteristic).

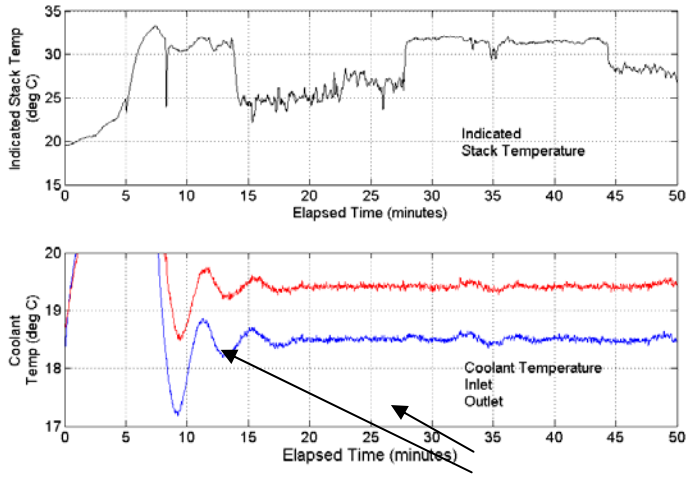

(a) open-circulation configuration

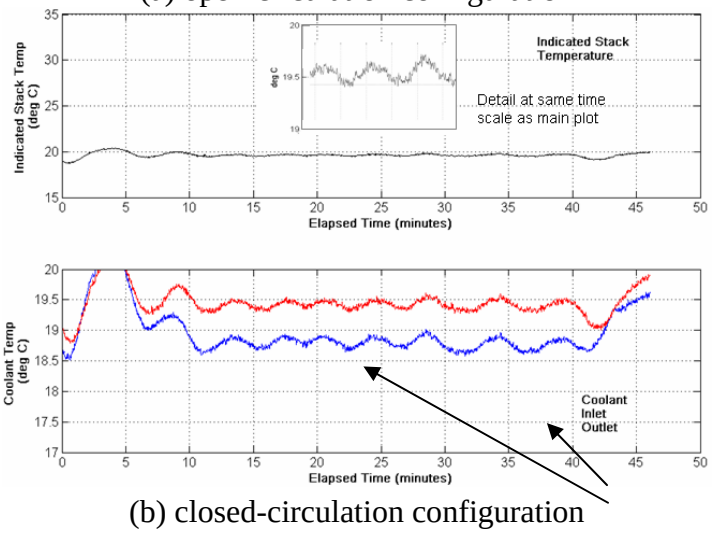

(b) closed-circulation configuration

Figure 3. Ultramill temperatures during operation with open-circulation cooling measured during operation with open and closed circulation arrangement (400 V_{PP} at 1 KHz)

3.3.2. SURFACE FINISH MEASUREMENTS

Flat features (1 mm long x 0.5 mm wide) were raster machined on a copper substrate while collecting Ultramill temperature data. The flats required 100 passes and each took approximately 8.2 minutes each. Three flats were cut using open-circulation cooling and 4 flats with closed-circulation cooling: two at the normal flow rate of 0.4 L/min for open-circulation cooling, one at 0.8 L / min and one at 0.16 L/min. The surface roughness of the parts was measured using white-light interferometry over the central portion of the flats (0.5 mm long x 0.4 mm).

Figure 4 shows RMS figure error as a function of the RMS variation of the stack temperature during machining for open and closed circulation tests. It shows that with open-circulation cooling, RMS stack temperature variation is considerable within a single machining run, ranging from 0.5 ˚C to 1.6 ˚C. The wide variation in RMS temperature between tests indicates that flow control is a problem and the system lacks repeatability. However, this has little effect on the figure error which stays around 17 nm. Using closed-circulation cooling, the RMS stack temperature variation is reduced to approximately 0.1 °C with little variation between tests. But again, the figure error remained the same. However, when the flow rate is dropped or increased beyond the 0.4 L/min, the figure error increased. The reason for this is the tuning of the temperature control system on the Thermocube. It has been optimized for the 0.4 L/min flow of the open circulation configuration and temperature variations occur if that flow is changed. Additional tuning of the controller could be performed but the 0.4 L/min was deemed acceptable.

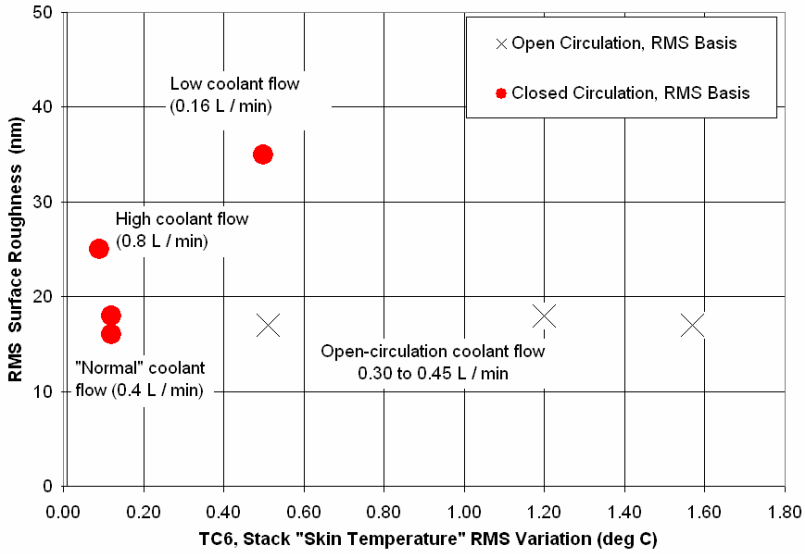

Figure 4. Comparison of surface roughness and form error as a function of circulation type with Ultramill operating at 400 V_{PP} at 1 KHz

3.3.3. CAPACITANCE GAGE TESTING

For capacitance gauge testing the diamond tool is replaced by an aluminum target of approximately the same mass. The capacitance gauge is fixed to the X-axis of the diamond turning machine. The average distance between the target and the cap gage (after the elliptical vibration motion is removed) is used to track the toolholder position in the depth of cut direction as a function of time. Cap gauge testing has two advantages over cutting flats: 1) the test duration can be set independent of the part size and 2) the capacitance gauge data is continuous in time rather than compromised by the raster scan pattern that may partially obliterate one pass by subsequent crossfeed passes.

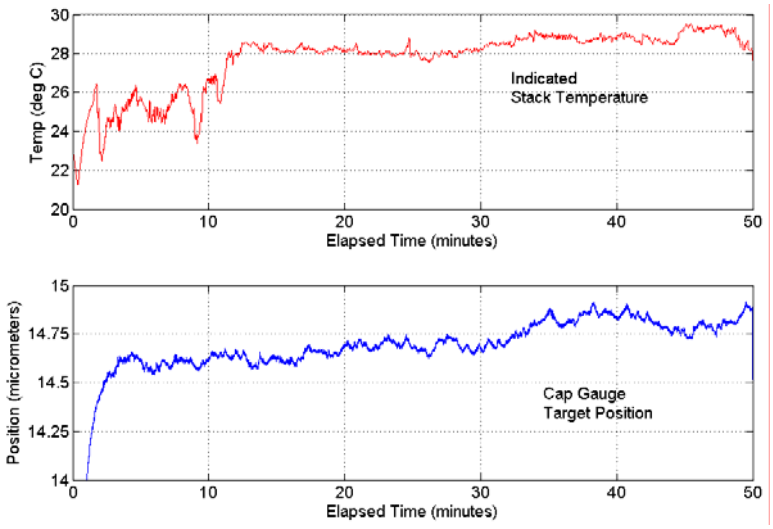

Figure 4. Capacitance gauge test for open-circulation cooling with Ultramill operating at 400 VPP and 1 KHz.

Figure 5 shows results for an open-circulation test of approximately 50 minutes duration. The top panel shows the stack temperature while the bottom panel shows the position of the cap gauge target relative to the location when the Ultramill is powered down. An increasing value for target position reflects motion toward the capacitance gauge probe, equivalent to thermal expansion of the tool in the direction of greater depth of cut. The stack temperature reached an approximate steady state at an elapsed time of approximately 12 minutes and then followed the stack temperature. The total expansion of the tool is on the order of 15 µm so it is essential that the system reach equilibrium before the cutting experiment is started. Capacitance gauge testing has not been completed for the close-circulation cooling configuration.

3.4. CONCLUSIONS

Open and closed circulation schemes have been studied on the Ultramill. The conclusions of this study include

- Closed-circulation cooling provides greater stack and coolant temperature stability when the coolant flow rate is maintained at approximately 0.4 L / min or greater.
- Closed-circulation cooling does not change the form error compared to open-circulation
- The Thermocube cooler was tuned for a flow rate of 0.4 L/min and that appears to be a reasonable flow rate for cooling the piezoelectric stacks.

4 FRESNEL LENS FABRICATION AND TESTING

Alex Sohn
PEC Staff Member

4.1. BACKGROUND

In the process of developing Fresnel lenses for scanning systems, it has been necessary to fabricate and test a number of Fresnel-type surfaces. A few structures were commercially available and tested as purchased, but the difficulty in measuring these surfaces as well as lack of availability of specific shapes such as constant-depth aspheric Fresnels and anamorphic surfaces has made it necessary to fabricate these. Initial testing included a Fresnel prism and a conical-groove constant-spacing Fresnel lens. Added to this was the fabrication and testing of a Fresnel lens with a true aspheric profile and constant-depth grooves.

4.2. FABRICATION

In response to the poor performance of the conical groove Fresnel lens in section 1.4.2., it was decided that a true aspheric-profile, constant groove depth Fresnel lens would be designed and diamond turned. The setup and process are described below.

4.2.1. DIAMOND TURNING SETUP

A 97 µm radius diamond tool was used to turn a 0.100" thick aspheric groove Fresnel lens in Plexiglas PMMA. Final feedrates of 2.5 µm per revolution were used to obtain a theoretical finish of 10 nm P-V. As the figure shows, an air ionizer was used to prevent static from binding chips or damaging the tool through electrostatic discharge. Figure 1 shows the result of the machining process.

Figure 1. Finished aspheric groove PMMA Fresnel lens.

4.2.2. SURFACE FINISH

Initial surface finish measurements produced inconsistent results, with it becoming apparent that the finish pass was not removing all of the tooling marks from the roughing pass. While this should not happen even with a 1 µm depth of cut on the finish pass, the final part was made with two finish passes: one at 5 µm D.O.C. and the last at 1µm D.O.C. The resulting surface is shown in Figure 2 where the surface finish over the area shown is 16 nm RMS.

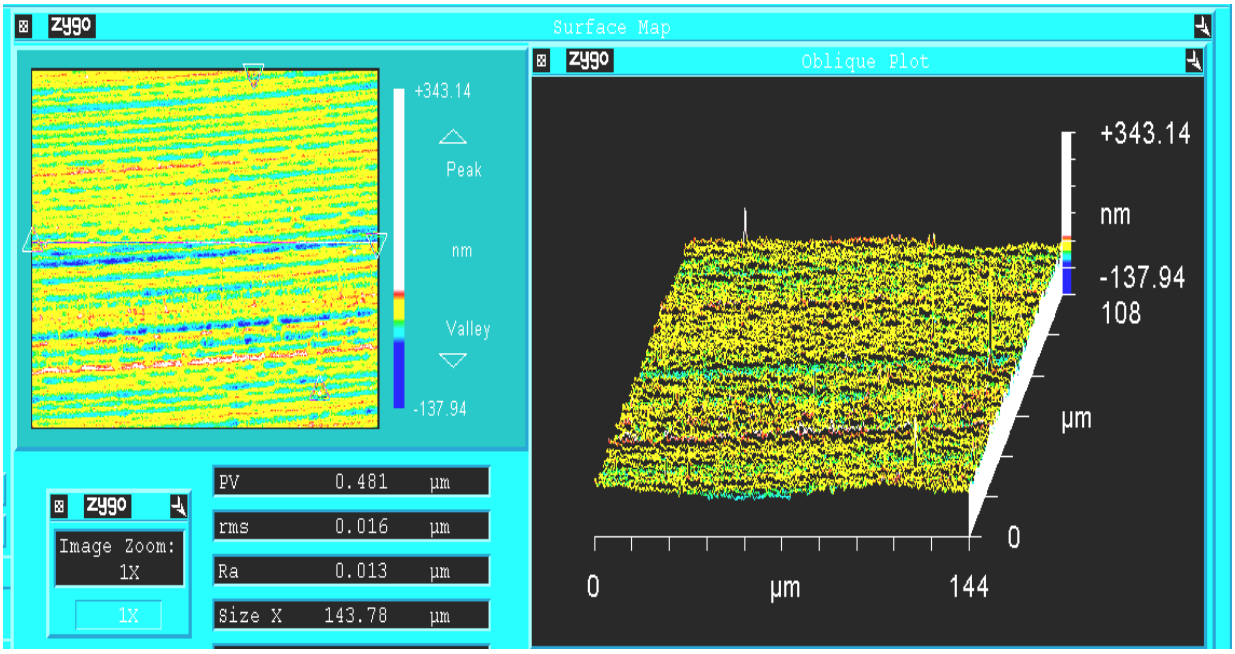

Figure 2. Surface finish of plastic aspheric Fresnel lens is 16 nm RMS.

4.3. TEST SETUP

The test will to examine the influence of Fresnel lens grooves on the spot size of a focused laser beam. As shown in Figure 3, a collimated laser beam is focused by a lens onto a camera array. A 200 mm focal length lens focuses the 5 mm diameter beam to the location of the focal plane of the camera. Here, a CMOS array will collect image data. Early experiments revealed that the 1 mW source was too intense and was causing saturation of the camera array. Using silicon mirrors with a much lower reflectance in the visible spectrum as fold mirrors accomplished this attenuation without unduly affecting the profile of the beam. For measurements of the aspheric Fresnel lens, a translation stage allows the Fresnel lens to be translated together with the camera at relatively precisely spaced intervals. This allows measurements at regular intervals along the aperture of the lens.

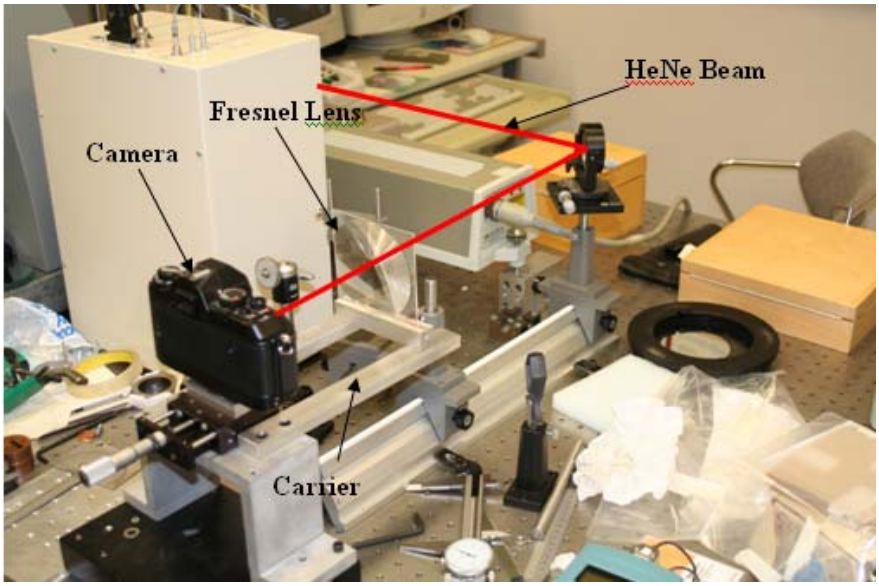

Figure 3. Experimental test setup

4.3.1. FOCUSING TEST

As part of the initial setup, the initial spot size as a result of the glass biconvex focusing lens (FL = 200 mm) was measured to establish a baseline for the tests. The tests were carried out by focusing the beam on the shutter surface of the camera. The results are shown in Figure 4. Since the camera was already set for the shortest exposure, the fold mirrors in the setup were replaced with silicon wafers (reflectance ~20%) to attenuate the beam. Additionally a neutral density filter was used to further attenuate the beam. As Figure 5 shows, the spot size is approx 80 µm FWHM.

Figure 4. Image spot from a 200 mm f.l. lens with a suitably attenuated beam.

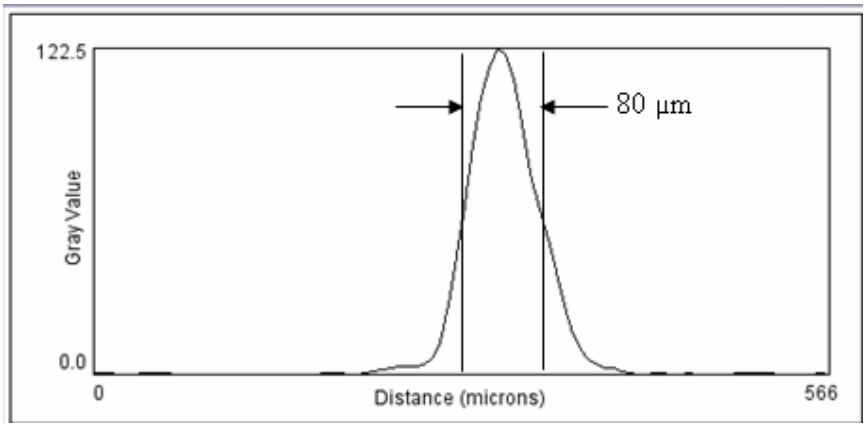

Figure 5. Intensity of spot shown in Figure 4. FWHM spot size is 80 µm.

4.4. MEASUREMENTS

Using the setup described in Section 4.3, both a conical groove Fresnel lens and the aspheric groove lens were tested. The results of the aspheric lens are presented here.

4.4.1. INCIDENT BEAM

The small aperture beam as measured through diamond-turned PMMA flat shown in Figure 6. The diameter of the beam is 1.4 mm FWHM. The same measurement was performed on the large aperture beam as shown in Figure 7 resulting in a beam diameter of 2.8 mm FWHM. Clearly, the beams are not an ideal Gaussian form, but have some lobing and structure. This may need to be considered in future measurements, though it appears to have minimal impact on these experiments as evidenced by the small spot size in Figures 4 and 5.

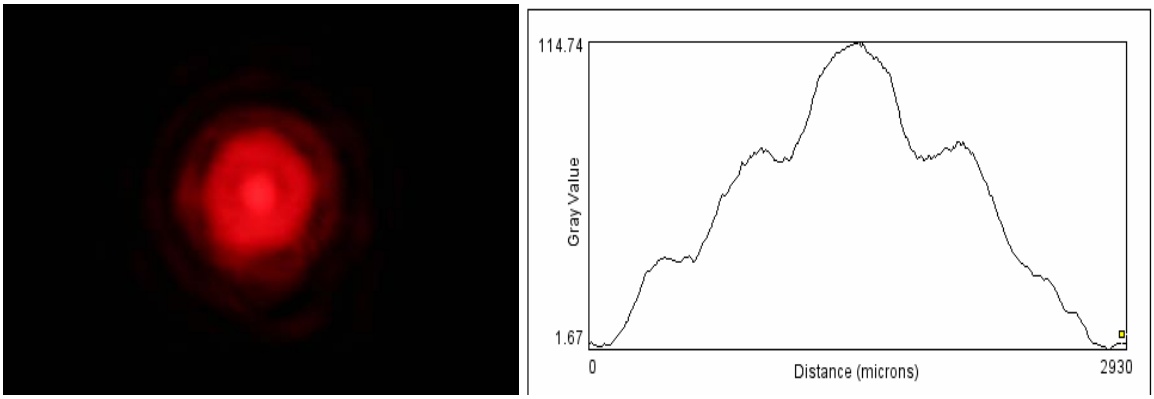

Figure 6. Incident beam with small aperture (FWHM =1.4 mm)

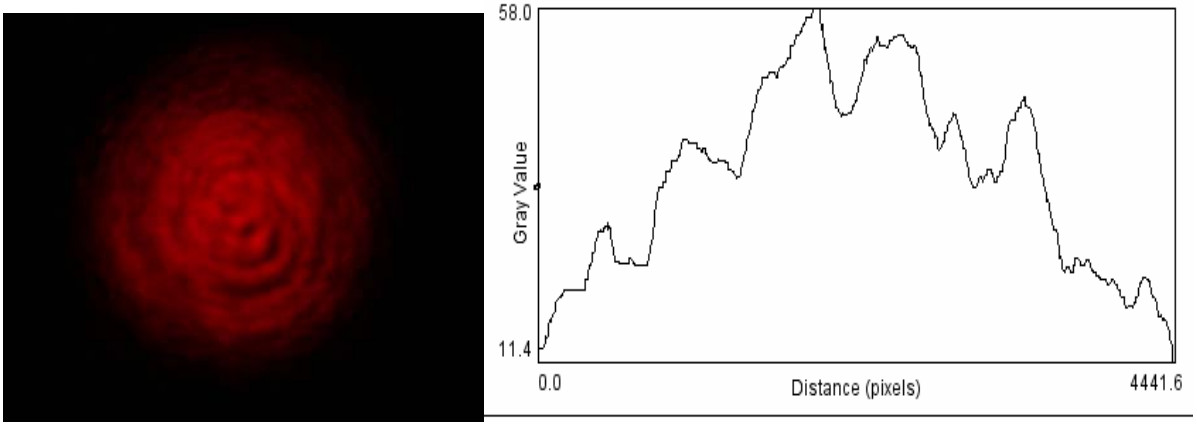

Figure 7. Incident beam with large aperture (FWHM =2.8 mm)

4.4.2. ASPHERIC GROOVE LENS

The Fresnel lens was inserted into the holder and centered with the grooves facing away from the camera. The 2.8 mm beam was manually scanned across the aperture from 0 to 43 mm in 2.54 mm increments. Several examples of these images are shown in Figures 8 through 10. Each individual image is 3.84 mm X 1.28 mm in size.

Figure 8. Spot formed by the center of the lens when illuminated with the large aperture beam shown in Figure 7. Images are shown as negatives for clarity.

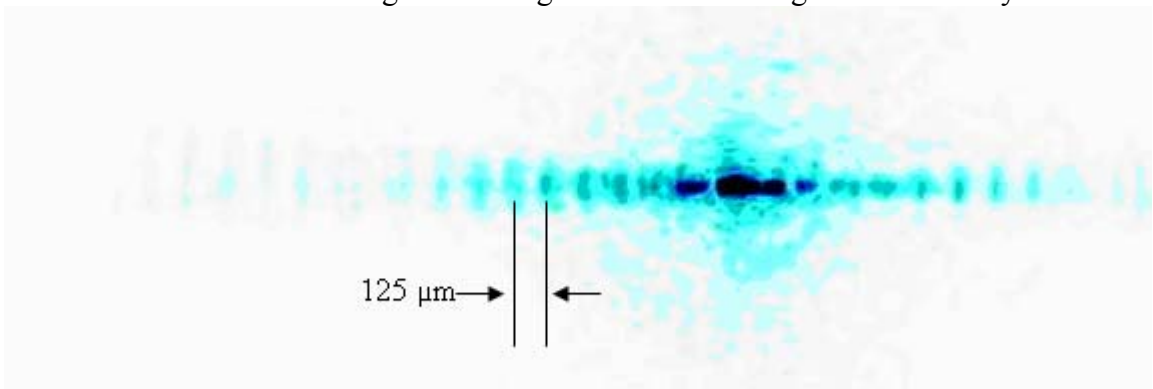

Figure 9. 22.86 mm off-axis, the fringe spacing is 125 µm. This corresponds to the groove spacing of 1 mm when calculated using Equation (1).

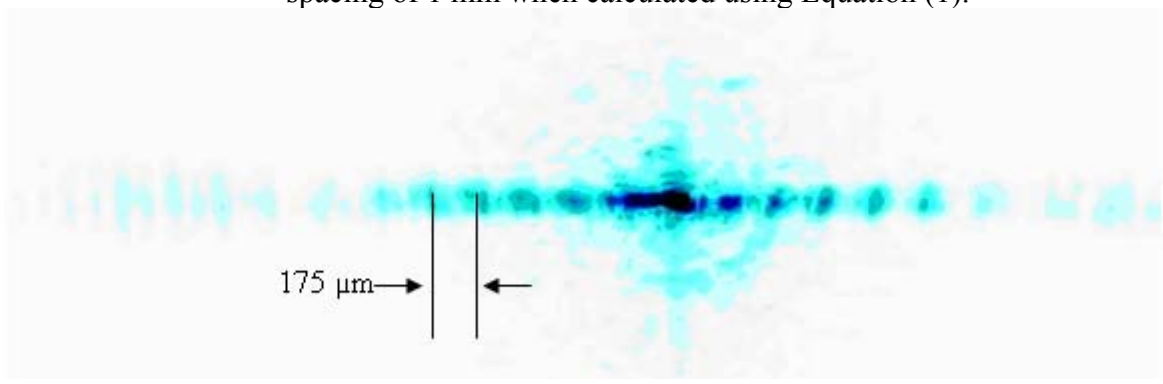

Figure 10. 30.48 mm off-axis, the fringe spacing is 175 µm. This corresponds to the groove spacing of 0.75 mm when using Equation (1).

4.4.3. DIFFRACTION

The difference in Figures 9 and 10 with respect to Figure 8 are the regularly spaced patterns in the focused beam which change as a function of the spacing of the Fresnel segments (see Section 1 for more details of the lens design). These patterns are assumed to be due to diffraction from the discontinuities formed by the grooves of the lens.

To estimate the spacing of the features, the equation for far field (Fraunhofer) diffraction is expressed as:

$$a \sin\theta = \lambda m \tag{1}$$

where a is the grating period, θ the diffraction angle, m is the diffraction order and λ is the incident wavelength. In the case of Figure 10, the spacing of the segment (*a)* is 1.1 mm at 22.86 mm radius on the lens shown in Figure 3 and the source is a HeNe laser of Figure 7 (λ = 632.8nm). Solving for θ and calculating the spacing of the first order fringes at 200 mm (distance from the lens to the camera), the feature spacing should be 136 µm.

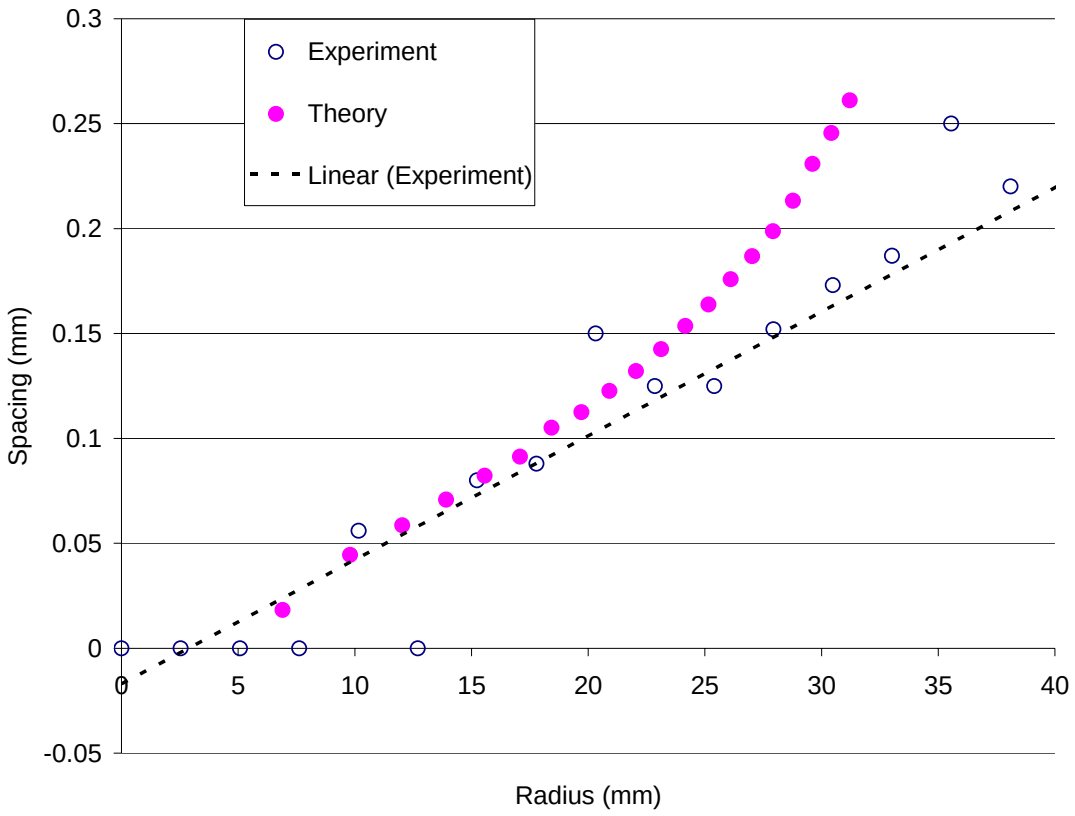

Figure 11. Plot of radial position of the incident beam on the aspheric Fresnel lens vs. spacing of the dominant spots produced by diffraction.

Figure 11 compares the spacing of the features from the experiment with those estimated from Equation (1). At small radii, the beam size (2.8 μm) is smaller than the size of the Fresnel segment and the diffraction effects do not occur. As the radius becomes larger, the spacing of the segments becomes smaller and the beam begins to overflow onto adjacent segments. At 12 mm radius the beam covers only one segment but at 27 mm radius, it covers 3 segments. The comparison of the estimated spacing from the diffraction equation and the measured feature spacing in Figure 11 are close at low radius but diverge from the predicted values as more segments are included. Clearly the simple diffraction equation does not explain the measured features nor does it lead to a design process to develop more efficient Fresnel lenses. A more complete diffraction analysis of the lens is under construction and will be used to develop the next generation scanning lenses.

4.5. CONCLUSIONS

An aspheric Fresnel lens was fabricated and was shown to produce a spot. A significant spreading of the spot into diffracted spots off-axis was shown to be the result of diffraction. A thorough analysis for all spots in the images grooves is somewhat more complicated due to the fact that the beam straddles more than one groove. Multiple diffraction angles as well as interference create multiple sub-spots and fine structure. A more thorough diffraction analysis is needed to explain these finer points. Armed with this knowledge, the next set of lenses that will be designed will be less influenced by diffraction and, hence, exhibit smaller spot sizes.

5 HIGH PRESSURE PHASE TRANSFORMATION OF SILICON

Timothy Kennedy
Graduate Student
Dr. Ron Scattergood
Professor
Department of Materials Science and Engineering

5.1 INTRODUCTION

Diamond cubic silicon (Si-I) is a brittle material under standard temperature and pressure, but when exposed to a high pressure environment the crystal structure transforms into a ductile β-Sn metallic phase (Si-II). Once the Si-II is unconstrained it back transforms into multiple forms of Si. The transformation schedule of silicon depends on loading, unloading, and temperature, Figure 1. This transformation allows silicon to be machined without brittle fracture occurring, but the back transformation alters the subsurface (5 nm to 400 nm in depth). This alteration can be divided into two layers: an amorphous layer and a damage layer. The amorphous layer extends from the surface down as far as 100 nm; this is the byproduct of the back transformation process which creates amorphous silicon (a-Si). Below the amorphous layer a damage layer extends another 400 nm; this layer is comprised of dislocation structures. Recently it has been shown through transmission electron microscopy (TEM) that depending on the machining technique and other parameters the damage layer can be eliminated.

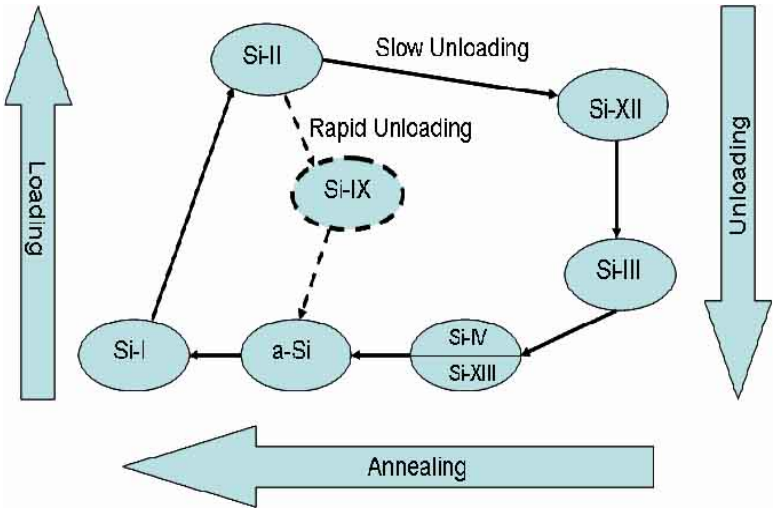

Figure 1. Silicon transformation schedule.

5.2 SILICON SAMPLE PREPERATION

Starting with an as received (100) oriented silicon wafer that had been chemically mechanically polished (CMP), a 10 mm by 20 mm rectangle is cut out of the wafer so that the <110> type direction is along the 10 mm width. Different crystal orientations are available but it has been shown that (100) oriented silicon along the <110> directions provides the best ductility. The tools used were 3 mm round nose diamond with -30° and -45° rake angles, from two different vendors (IMT and Edge Tech). Samples are machined using a traditional t-lathe setup and a parallel fly cutting setup. Only the fly cutting used both vendors' tools, and it is important to note that when the samples were fly cut that all the tools were freshly sharpened.

5.3 TEM RESULTS:

5.3.1 T-LATHE SET UP

Previous TEM results from t-lathe machining showed the existence of a damage layer below the a-Si layer. Lathe machined samples used an IMT tools at 1 μm/rev and 5 μm/rev. Figure 2 was machined at 5 μm/rev and is a representation of lathe machined silicon with IMT tools showing dislocations and slip planes.

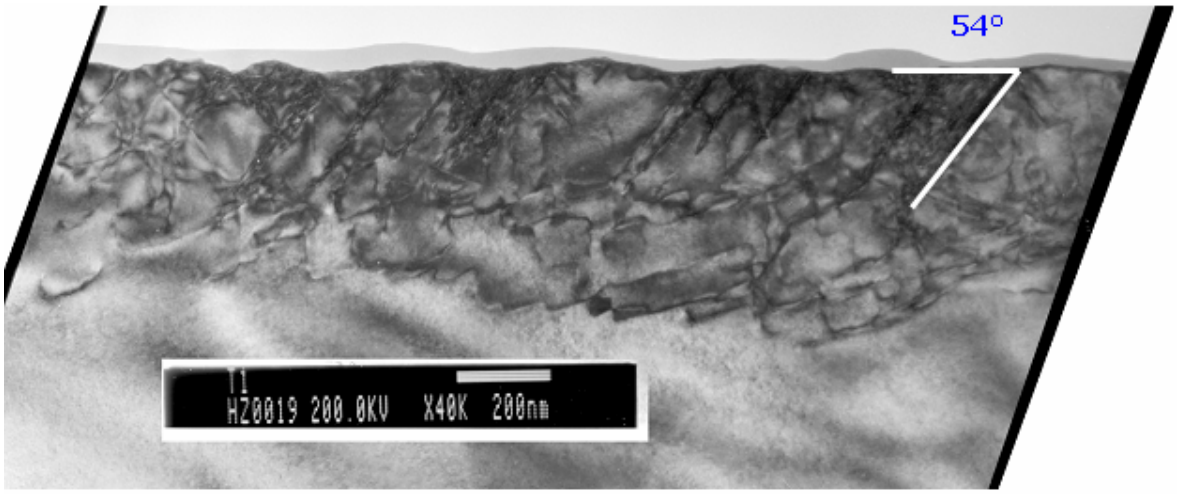

Figure 2. TEM micrograph at 5 μm/rev with an IMT -30° tool. The (111) slip system angle is shown along with the a-Si layer and the dislocation microstructure.

5.3.2 FLY CUTTING SET UP

When the machining technique is switched to parallel fly cutting a change in the subsurface was evident. Figures 3 and 4 were fly cut at 5 μm/rev with an IMT -30° tool, and there is no damage

layer beneath the a-Si layer when compared to Figure 2. Even the a-Si layer is dramatically thinner than previously measured.

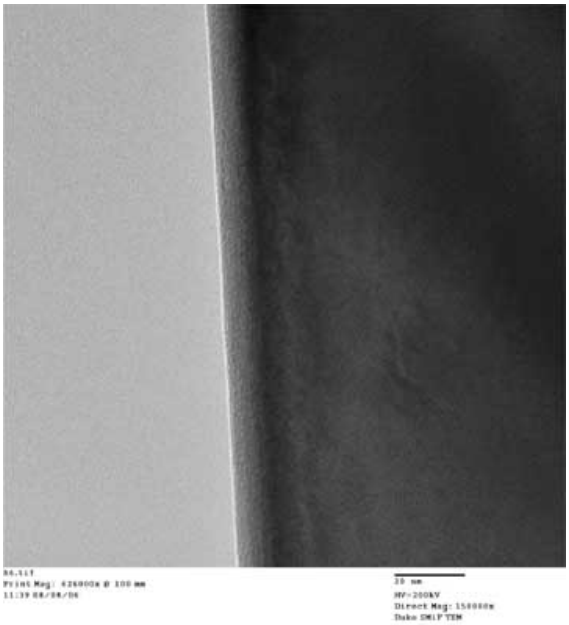

Figure 3. TEM micrograph fly cut at 5 μm/rev with an IMT -30° tool. Notice the lack of a damage layer.

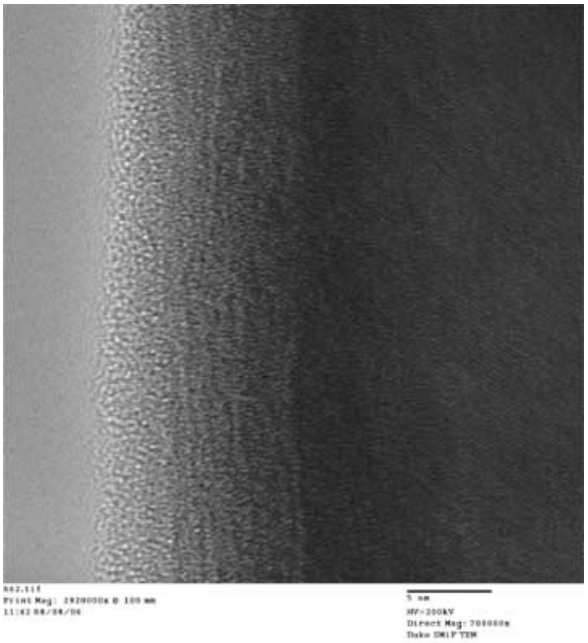

Figure 4. TEM micrograph fly cut at 5 μm/rev with an IMT -30° tool showing a higher magnification of the a-Si layer at the surface.

When the tool vendor is changed to Edge Tech the same microstructure is seen. Figures 5 and 6 were fly cut at 5 μm/rev with an Edge Tech -30° tool, and the same lack of dislocations and a thin a-Si layer is apparent.

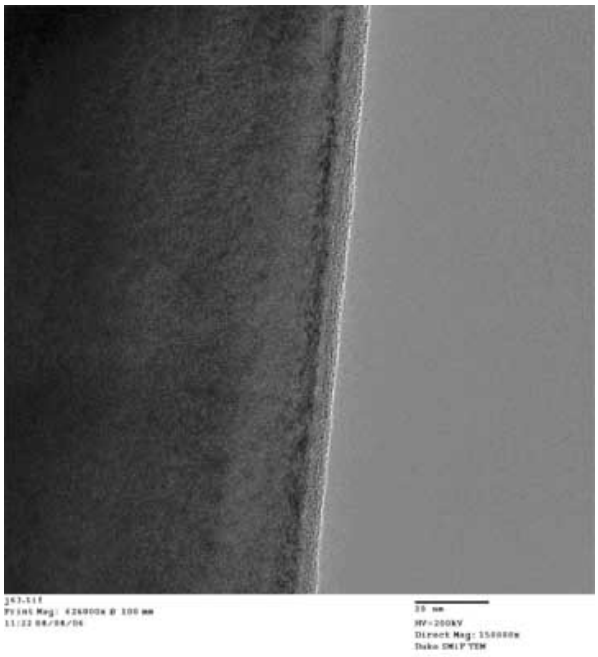

Figure 5. TEM micrograph fly cut at 5 μm/rev with an Edge Tech -30° tool. Notice the lack of a damage layer.

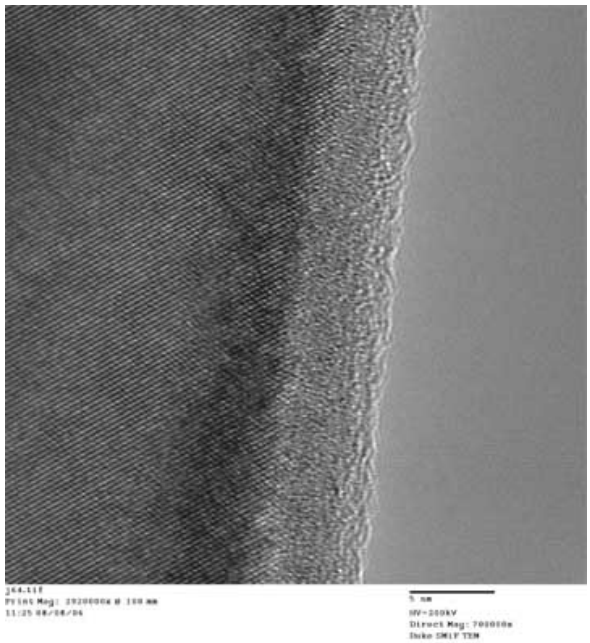

Figure 6. TEM micrograph fly cut at 5 μm/rev with an Edge Tech -30° tool showing a higher magnification of the a-Si layer at the surface.

When the feed rate is lowered to 1 μm/rev with an Edge Tech -30° tool nanocrystals appear below the a-Si layer, Figure 7. It is unclear how these nanocrystals were formed in the sample, since the same piece of silicon was used for the 5 μm/rev samples shown in Figures 5 and 6. As of now it is believed to be an anomaly. But if more samples at this cutting condition, both with the Edge Tech and/or IMT tool, show this phenomena then it will need further study.

5.4 MACHING TECHNIQUE COMPARISON

Beyond comparing t-lathe machining and fly cutting it is important to compare these results with the results found from CMP processing. It is interesting to compare these new TEM results to the as received CMP silicon wafer in Figure 7, which shows a nominal a-Si layer thickness of around 2 nm. It was previously thought that CMP was the only way to achieve optical surface finish with very little subsurface damage, but that has been proven not to be the case. On average there was a difference of 35 nm in the thickness of the a-Si layer between the lathe and fly cut samples.

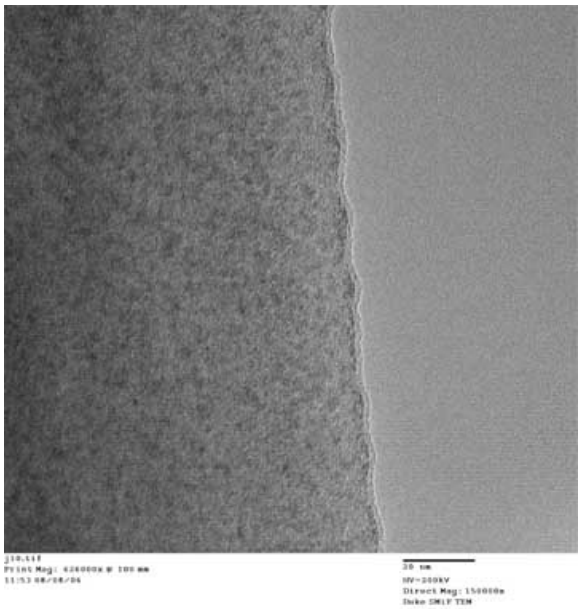

Figure 7. TEM micrograph of as received CMP polished silicon wafer.

5.5 CONCLUSIONS AND FUTURE WORK

It is highly unlikely that there is enough of a difference in machining techniques to produce the difference in their results. Since the samples that were t-lathe machined were done so with "dull" IMT tools, and the samples that were fly cut were machined with newly sharpened IMT and Edge Tech tools it seems that as of now tool sharpness plays a critical roll in the production of subsurface structures in machined silicon.

These new results also help to understand the deformation mechanism in machined silicon. There had been some doubt to whether a high pressure phase transformation (HPPT) occurred in the t-lathe machined samples due to the size of the damage layer. But using sharp tools and fly cutting it appears that an HPPT did occur due to the lack of a damage layer and the uniformity of the back transformed a-Si layer.

To ensure reproducibility, more silicon will be machined and examined in the TEM. Along with the reproducibility of the previous work, surface analysis and tool force measurements will be obtained on silicon. The most common brittle semiconductors that have been studied in machining experiments have been silicon, germanium, and silicon carbide. To add to this knowledge bank, it has been determined that lithium niobate should also be examined. Lithium niobate ($LiNbO_3$) is an important optical material, and it has been shown to have similar high pressure behavior when compared to silicon. To date there has been only one study of lithium niobate's machining behavior, and no studies to determine the subsurface created after machining.

6 RAKE ANGLE VARIATION IN DIAMOND TURNING

Alex Sohn
PEC Staff Member

6.1 INTRODUCTION

When turning non-rotationally symmetric (NRS) surfaces using a fast-tool servo (FTS), the rake angle of the tool effectively changes as a function of the surface slope. As fast tool servos find ever more applications and are pushed to ever larger strokes and higher operating frequencies, the diamond tools used on them tend to encounter larger variations in rake angle. Recent experiments at the Precision Engineering Center (PEC) have pushed this envelope to variations in rake angle of up to 90 degrees. The effect on figure, finish and tool life is substantial, so a quantization of the errors is needed. The varying tool forces are the main contributor to rapidly changing cutting conditions. These tool forces have been measured in various cutting experiments with the goal of determining optimum rake angles for machining. Large negative rake angles produce large thrust forces whereas large positive rake angles require large clearance angles and, hence, fragile tools. With advance knowledge of the tool forces and the material being cut, an optimum initial rake angle may be found.

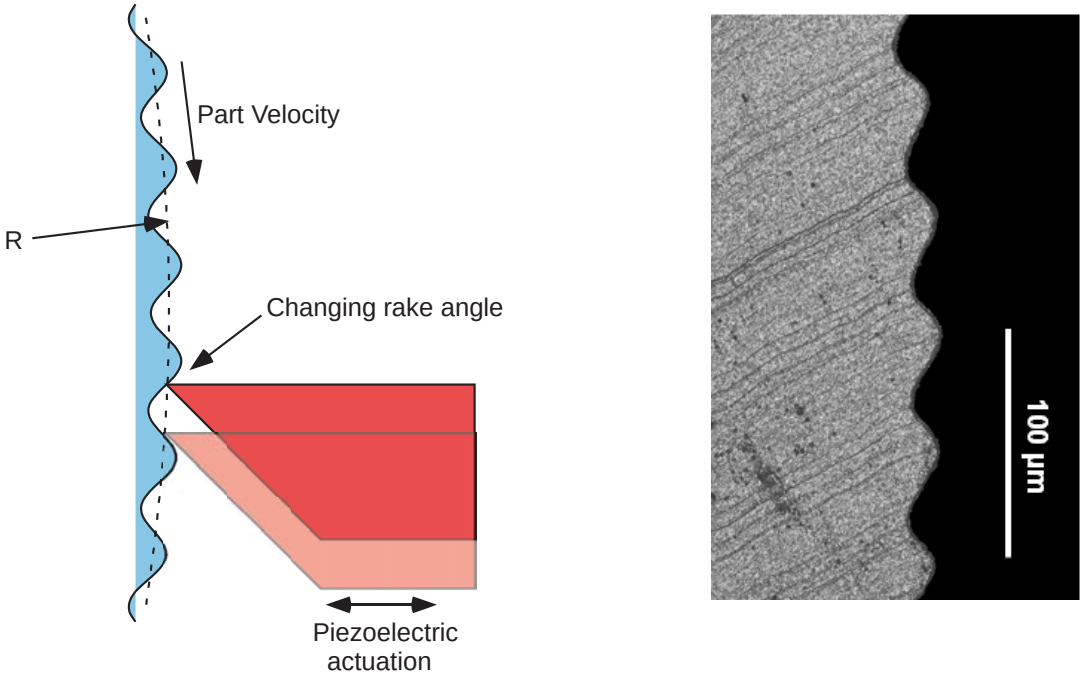

Figure 1. Sketch of cutting process and cross-section of finished sine wave surface with 360 periods of a 17 µm sine waves on a 6 mm dia. cylinder

The example case studied here involves a 6 mm diameter cylinder with sine waves machined around the periphery. This part was machined at the PEC with a piezoelectric fast tool servo of 20 µm range and 1 kHz bandwidth. A sketch along with a magnified cross-section is shown in Figure 1. Two observations in making these parts led to this investigation of tool forces: 1) significant distortion occurred in the shape of the sine waves and 2) abnormally high tool wear occurred even with the short cutting distances and the small depth of cut.

6.2 TOOL FORCE AS A FUNCTION OF RAKE ANGLE

To find the force variation involved in cutting these sinusoidally figured parts, the forces had to be measured. Previous investigations into tool forces at the PEC [1, 2] by Arcona and Drescher did not measure the effect of varying rake angles, though efforts to assess tool forces at normal (0º rake) incidence were successful.

The experimental setup used for measuring forces (Figure 2) involved placing a sample on a Kistler 9251A piezoelectric load cell and collecting force data while the sample was flycut. The interrupted cut avoided the problem of charge loss in the piezoelectric load cell, though some ringing at the beginning of each cut had to be truncated from the data. The sample was electroless nickel plated copper and was fixed while the rotating tool could be repositioned at varying rake angles. The tool clearance angle of 12º, however, limited positive rake angle measurements to 10º.

The measured cutting and thrust force orientations are shown in Figure 3. The force directions are fixed with respect to the surface of the workpiece as the tool is rotated through different rake angles.

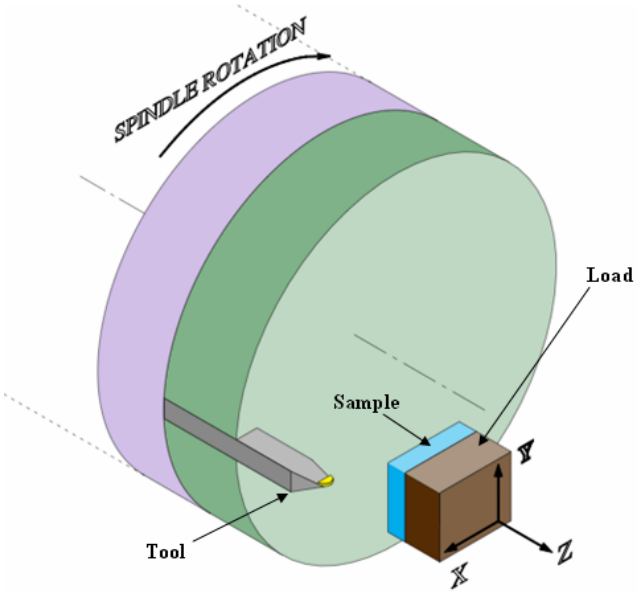

Figure 2. Schematic showing setup for tool force measurements

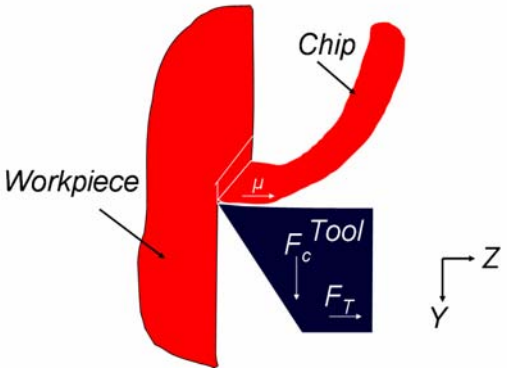

Figure 3. The cutting force (F_c) and the thrust force (F_t) are measured with respect to the shown axis orientations of the machine

A sample measurement is shown in Figure 4. The plot shows one pass over the sample at 0º rake angle. Data was collected at 5 kHz. Cuts were made with the tool positioned at 0º, 10º, -10º, -20º and finally 0º again. The freshly lapped tool had a conical nose radius of 0.5 mm. Each cut was performed with a 20 µm upfeed and a 10 µm depth of cut at 120 rpm spindle rotation. The final results for force measurements are tabulated in Figure 4. Each data point represents an average of 20 passes over the workpiece.

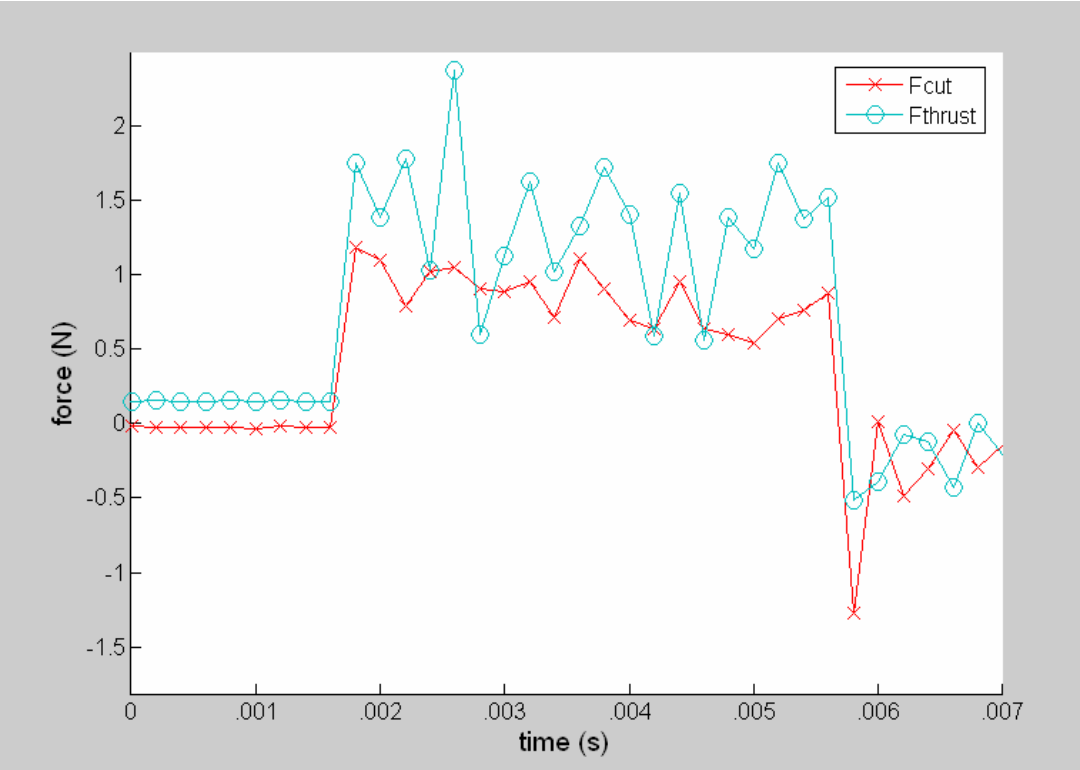

Figure 4. Sample force measurement at 0º rake angle

A least-squares 2nd-order polynomial curve fit allows extrapolation to larger rake angles. Future experiments using large-clearance tools and a larger adjustment range of tool angle will actually allow data collection at rake angles larger than 20º.

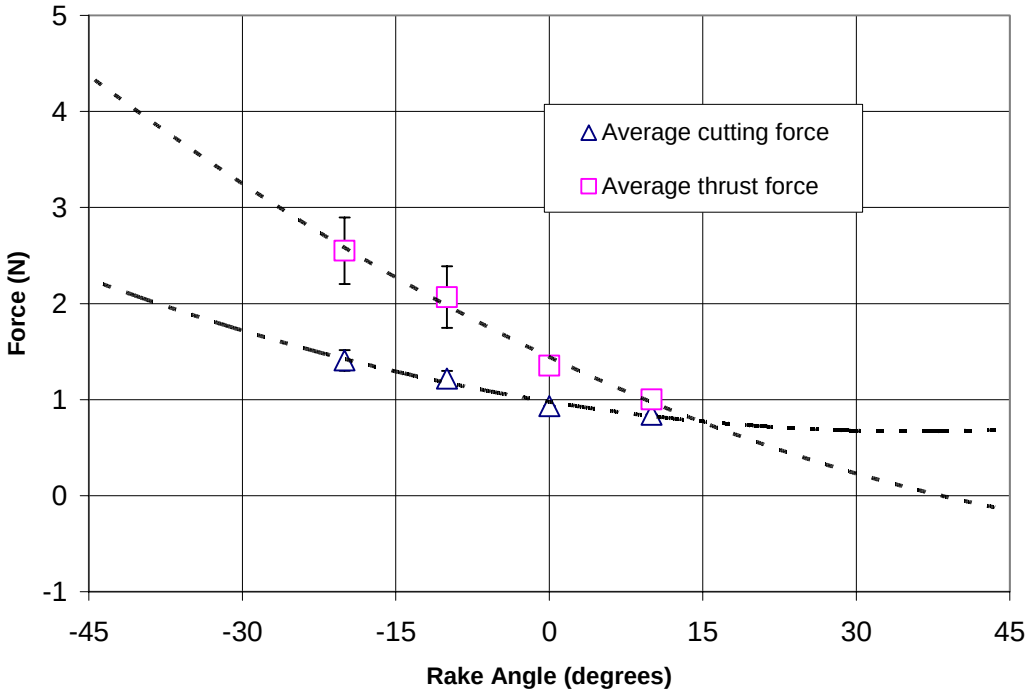

Figure 5. Force variation as a function of rake angle. The dashed lines are least-squares polynomial fits to the data and are extrapolated to ±45 º.

6.3 IMPACT ON FIGURE ERROR

While tool forces are always present in machining, constant forces usually have little impact on figure error, particularly in ordinary turning applications when stiff toolposts are used. Fast-tool servos typically are limited in their static stiffness, however, and varying forces can cause them and the workpiece to deflect. Particularly on small parts, compliance in the material can be significant, causing a figure error. Test parts were structured with a 16µm sine wave with ±45° rake angle variation. The part was a 6 mm dia. electroless nickel plated brass cylinder. Modeling the cylinder as a cantilever beam with a length of 20 mm, its stiffness will be 2.75 N/µm and the deflection of the part can be calculated from the experimentally obtained tool forces. Calculating deflection from this and correlating to the measured forces yields a perturbed sine wave as shown in Figure 6. This distorted sinusoidal shape is very similar to that shown in Figure 1 and when superimposed onto the measured data follows the shape of the actual part. This is illustrated in Figure 7.

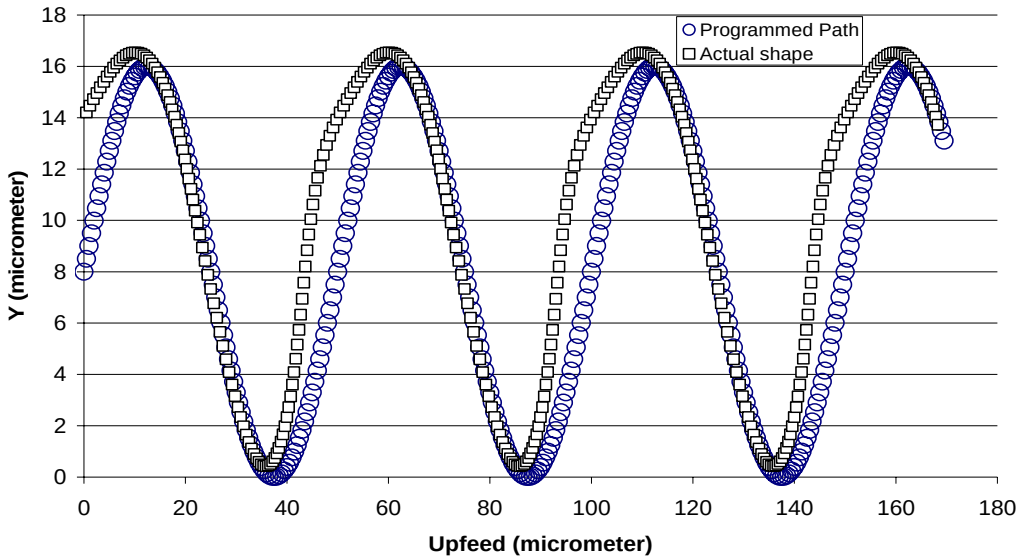

Figure 6. Perturbed shape of the sine waves machined on a 6 mm diameter, 20 mm long brass cylinder. The programmed ideal path is shown for reference.

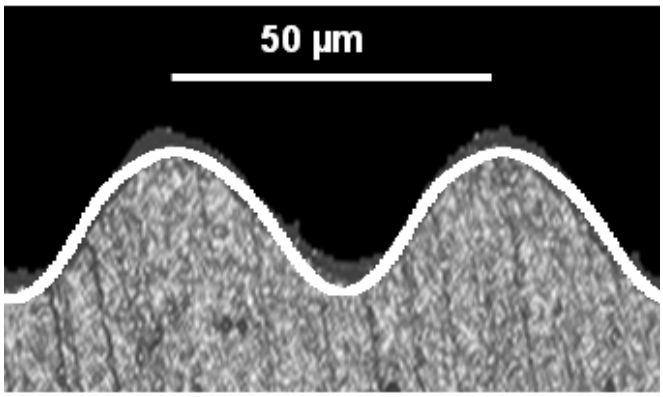

Figure 7. The calculated perturbed tool path from Figure 6 superimposed on Figure 1

6.4 TOOL LIFE

Significant wear was noted on the tool used to machine the sine wave parts. The distance cut was less than 500 m yet the tool surface showed signs of wear. Ordinarily, this cutting distance in electroless nickel would not lead to appreciable wear of the tool. However, with the extreme clearance angle of 50° resulting in an included angle of only 40°, the edge becomes quite fragile. This geometry of the tool was based on the conventional non-ferrous diamond turning practice of starting with a 0° rake angle tool. For the application described here, the clearance angle must be at least 45°; however; the initial rake angle could be anywhere from 0 to – 45°. The tool force measurements (Figure 5) show that the cutting forces drop as the rake angle goes from negative to positive values.

The optimum geometry can be determined by applying tool force data to different tool geometries and evaluating the internal stresses in the diamond. Initial assessments using COSMOS finite element software and the experimental force values of Figure 5 are shown in Figure 8. Figure 8(a) is a result of applying the forces measured at - 20º to the tool. The maximum stress occurs at the depth of cut away from the endge of the tool and is 5 GPa. Figure 8(b) shows the results when the forces measured for 0º rake angle are applied and the peak value is 2.9 GPa. The vector sum of the tool forces at each rake angle and the stress on the tool are proportional. In addition, internal shear stress increase as the clearance angle becomes more negative.

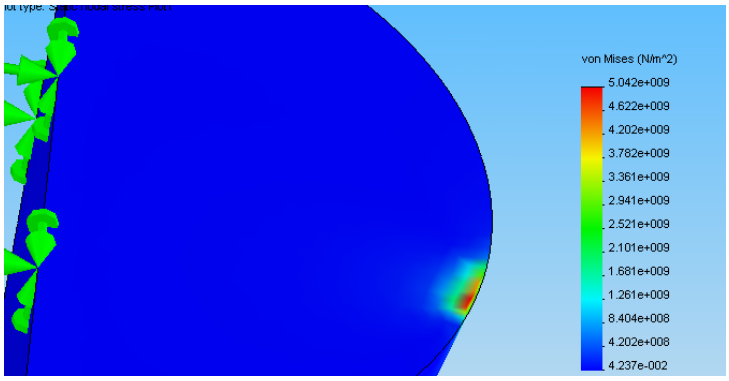

(a) - 20º rake angle, maximum stress is 5 GPa

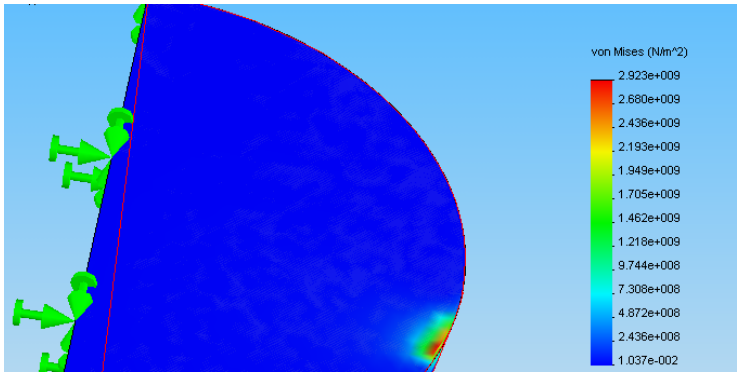

(b) 0º rake angle, maximum stress at 2.9 GPa

Figure 8. FEA of diamond tool and maximum stresses

6.5 CONCLUSIONS

The role of a changing rake angle in machining free-form optics is rarely addressed. However, as tool excursions and, hence, surface slopes increase, the impact of rake angle variation cannot be ignored. This will be true both from the standpoint of static deflection of the workpiece and tool as well as the impact on the life of the tool. The preliminary results presented here represent the first step in an effort to understand the impact of varying rake angles in diamond turning. The resulting knowledge will lead to methods for combating the negative effects of this phenomenon, ultimately, better more cost effective free-form optics.

REFERENCES

1. Arcona, C., “Chip Formation and Surface Finish in Diamond Turning”. PhD Dissertation, NC State University, 1996.

2. Drescher, J. P, “Tool Force, Tool Edge and Surface Finish Relationships in Diamond Turning”, PhD Dissertation, NC State University, 1992.

7 ELLIPTICAL VIBRATION-ASSISTED MACHINING

David Brehl
Graduate Student
T.A. Dow
Professor

7.1 BACKGROUND

The objective of the current research is to use Elliptical Vibration-Assisted Machining (EVAM) to make sub-millimeter scale structures typical of those found in micro-optical, micro-fluidic, and MEMS type devices. This goal requires achieving the following capabilities:

- create sculpted 3-D and arbitrary non-rotationally symmetric geometries
- optical quality surface finish
- aspect ratios of >0.1
- machine multiple materials, including ferrous metals and brittle materials that cannot be economically cut by conventional diamond turning

Figure 1 shows the operation of the Ultramill which consists of a pair of piezoelectric actuators and a T-shaped tool holder that can produce elliptical motion of the tool. It can operate at up to 4 KHz (below its first natural frequency) and the shape of the motion can be modified by changing the signals to each actuator.

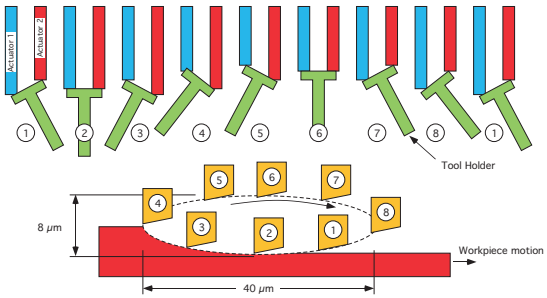

FIGURE 1. Elliptical motion produced by a pair of actuators and a T-shaped tool holder

Early experiments used the Ultramill EVAM tool to make geometrically simple structures such flats in copper, aluminum and SiC. These parts included optical quality flats and low relief binary structures with arbitrary geometry. This work showed that the Ultramill can achieve surface finishes better than 15 nm RMS in a variety of materials and a figure error less than λ/4.

In the next phase of work the Ultramill will be used to make functional structures. A beam splitter project is described next. It improves upon existing concepts by using the Ultramill to machine complex reflecting surfaces which eliminate the need for collimating refracting elements.

7.2 FIBER OPTIC BEAM SPLITTER[1]

The fiber-optic beam splitter will be used to demonstrate the ability of the Ultramill system to make a functional device that requires fabrication of optical surfaces with complex geometry. Figure 2 shows a beam splitter design that is based on refracting collimating optics. A light beam exits the source fiber in a diverging cone. The divergence angle is approximately the same as the required angle of acceptance for light entering the inlet of the receiving fibers. Light approaching at greater than the angle of acceptance is not transmitted by the fiber and is wasted. To keep coupling losses small, ball lenses are used to collimate light emanating from the source fiber before it reaches the beam splitter mirror, and then to focus the light on the entrance plane of the receiving fibers.

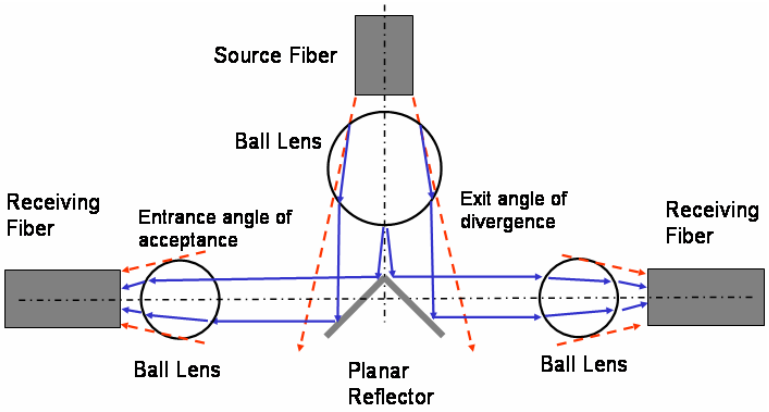

Figure 2. Typical refractive type beam splitter. Ball lenses are used to collimate the divergent light rays from the source fiber and focus them on the receiving fibers.

An alternate concept, making use of the capability of the Ultramill, is shown in Figure 3(a). The beam splitter mirror is concave and curved in three dimensions. It focuses the diverging beam from the source fiber onto the receiving fibers. This approach eliminates refracting elements such as ball lenses which must be precisely positioned relative to the fibers for maximum coupling efficiency. The number of optical components is reduced from four to just one. The semi-major axis length A and semi-minor axis length B can be selected using the relationship $B^2 = A^2 - F^2$, where F is the distance of the foci from the center of the ellipse. Once the ellipse

[1] T. Bifano of Boston University suggested the fiber optic beam splitter using reflecting optics as a project for the Ultramill.

profile is established, the corresponding three-dimensional figure is obtained by revolving it around the major axis. The maximum radius of the ellipsoid's circular cross section is *B*, the length of the semi-minor axis.

The concept is designed around a commercially-available optical fiber with an active diameter of 0.486 mm and 61˚ acceptance angle as shown in Figure 3(b). The elliptical cross section has semi-major axis A = 2.38 mm and semi-minor axis B = 1.40 mm. The figure shows light originating at one focus behind the exit plane of the source fiber, emanating over the entire divergence angle, and being brought to the other focus at the entrance plane of the receiving fiber. To fabricate the beam splitter, only the indicated portion of the elliptical profile is needed, extending from the source fiber's centerline to the intercept point of the ray at the divergence half-angle with the ellipse. The required surface makes a circular curve into the plane of the paper, with maximum radius of 1.40 mm.

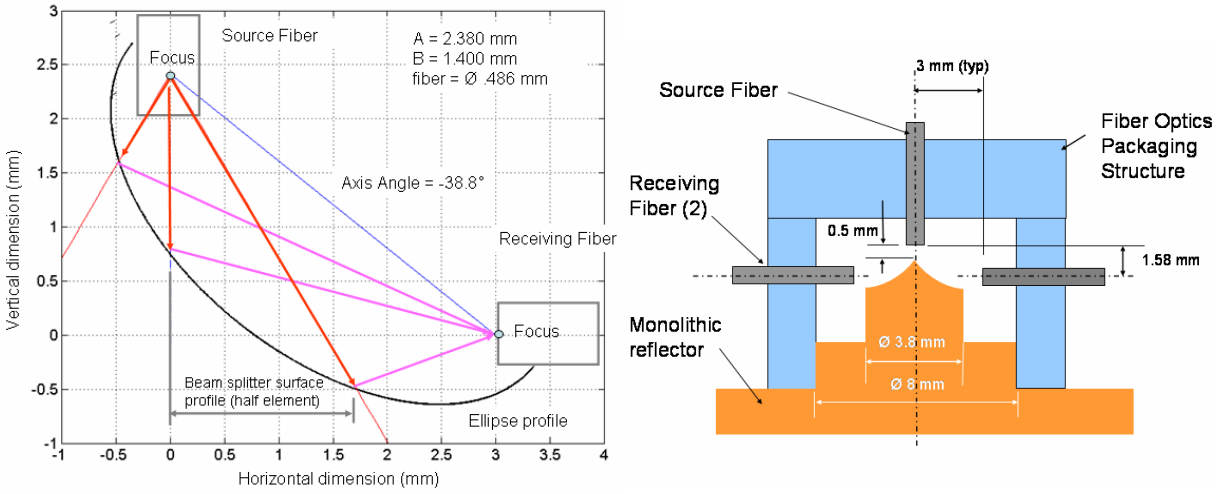

(a) (b)

Figure 3. (a) Development of reflector surface for the beam splitter, based on geometry of an ellipse with one focus located in the source fiber and the other focus on the receiving fiber. (b) Sectional view of beam splitter.

7.4 SPHERICAL SURFACE MACHINING EXPERIMENT

Before fabricating the beam splitter, the Ultramill was used to machine concave spherical reflectors of similar shape and sag. A spherical form was selected because the whole surface can be measured with the Zygo GPI interferometer rather than measuring cross-sections with the Talysurf. The part aperture diameter is 1.5 mm and the radius of curvature (-4.5 mm) was chosen so that such that surface angle was less than the 10˚ clearance angle of the cutting tool. The maximum sag of 63 µm multiple cuts was divided into several passes, each 11 µm deep. The finish pass was made at a nominal depth of 1 µm and required 150 raster passes at 10 µm

crossfeed spacing. Mineral oil was used as the lubricant and the part required 70 minutes to machine.

Figure 4 shows GPI interferogram of the spherical surface. It shows the departure of the machined surface from the intended spherical surface. The top panel is a contour plot of the error while the bottom panel is an oblique view of the error surface. There is a small ridge across the middle of the part caused by non-linearity in the ballscrew drive of the Z-axis. The Z-axis has to stop and move in the opposite direction while the X-axis moves at constant speed. This creates an error near the center of the part. In addition, there is some astigmatism (saddle shape) caused by lack of squareness between the X and Z axes and tool radius errors would also show up at this high resolution. Measurements will also be made on this surface using the Talysurf profilometer to understand how these features would be represented in those 2D scans.

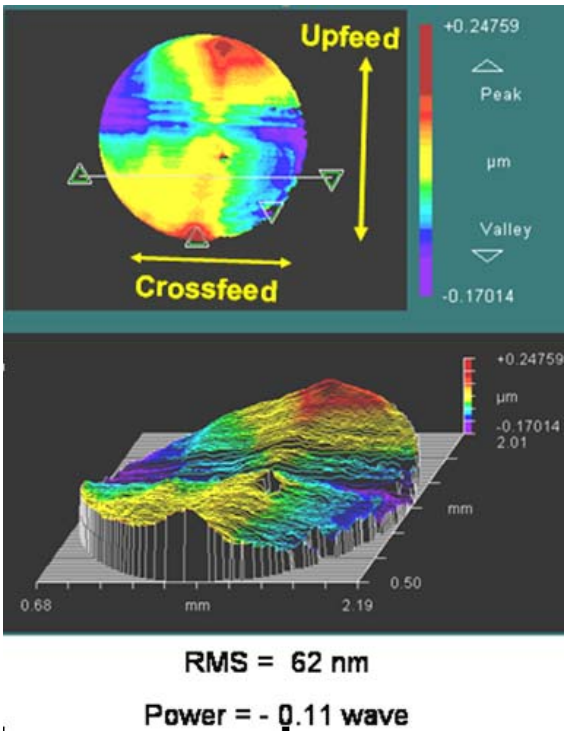

Figure 4. Interferogram of spherical copper surface machined using the Ultramill with a form error 62 nm RMS or λ/10. The errors in the surface show astigmatism and a central ridge feature.

7.5 CONCLUSIONS

The Ultramill EVAM tool can been used to make a variety of feature geometries, including flats, binary features, trihedrons, and sculpted 3-D features. A fiber optic beam splitter been designed which features ellipsoidal reflecting surfaces to be machined using the Ultramill. This concept eliminates additional refracting elements, such as ball lenses, used by existing beam splitter concepts for collimation. Concave reflecting surface with spherical form have been machined by the Ultramill to see the form errors that would be present in the elliptical sections. Several surfaces were machined and errors have been removed on successive parts, reducing the figure error to 62 nm RMS.

7.6 ACKNOWLEDGEMENT

Principal funding for this work is by National Science Foundation grant DMI-433215, monitored by G. Hazelrigg. Chardon Tool provided diamond tools for the experiments.

8 AUTOMATIC HANDLING TECHNOLOGY FOR HEMISPHERICAL SHELLS

Kenneth Garrard
Alex Sohn
Precision Engineering Center Staff
Stephen Furst
Graduate Student
Thomas Dow
Duncan Professor of Mechanical Engineering

8.1 BACKGROUND

A significant issue in the manufacture of thin-walled hemispherical shells is the uniformity of shell thickness after machining. Diamond turning lathes routinely produce spherical parts with form accuracy of λ/10; however machining both the inner and outer diameters of a shell to a concentricity of even 1 μm is a significant challenge. Transfer of the part between fixtures designed for machining the concave inner contour (IC) and convex outer contour (OC) typically requires manual intervention by a skilled operator. One of the surfaces must be machined to its final shape and finish first and is thus at risk of being damaged during the transfer, alignment and machining of the other surface. The goal is to produce a full hemispheric shell with concentric IC and OC of the correct radii using new agile, multi-function machining centers (e.g., Mazak Integrex series). Eliminating manual part transfer and alignment operations can result in significant cost savings and improved part accuracy. Automating the transfer of shells between spindle fixtures and correcting the radial shell alignment on the OC fixture is the objective of a new project sponsored by BWXT-Y12. This report describes progress during Phase I of this project – sensor selection, the data analysis algorithms that will be used and an error assessment of the expected system performance.

8.1.1 HEMISHELL TRANSFER

Figure 1 illustrates the hemishell transfer and alignment problem. In (a), the outer contour of a shell has just been machined and the task is to transfer to the shell to another chuck for machining the inner contour. The location of the two fixtures and their dimensions are known, but the location and outside radius of curvature of the shell (shown in green) is unknown. By probing the shell surface at the three numbered locations both of these unknown quantities can be found and the distance to move the shell toward the IC chuck calculated. Similarly, in (b) the

shell is shown on the IC fixture and is to be transferred to the OC fixture. The locations numbered (1) and (2) will be probed to find the distance from the mounting edge of the part to the OC fixture and to ensure that there is no interference between the raised center section of the OC fixture and the inside edge of the shell. In addition, probing locations (3) and (4) will allow the inside radius of curvature to be calculated. During transfer of the shell to the OC chuck the part may slip and become misaligned. However, shell runout can be easily measured by rotating the OC spindle with the probe near the equator (i.e., location (3) in part (a) of Figure 1). A repositioning mechanism will then push the shell back into alignment.

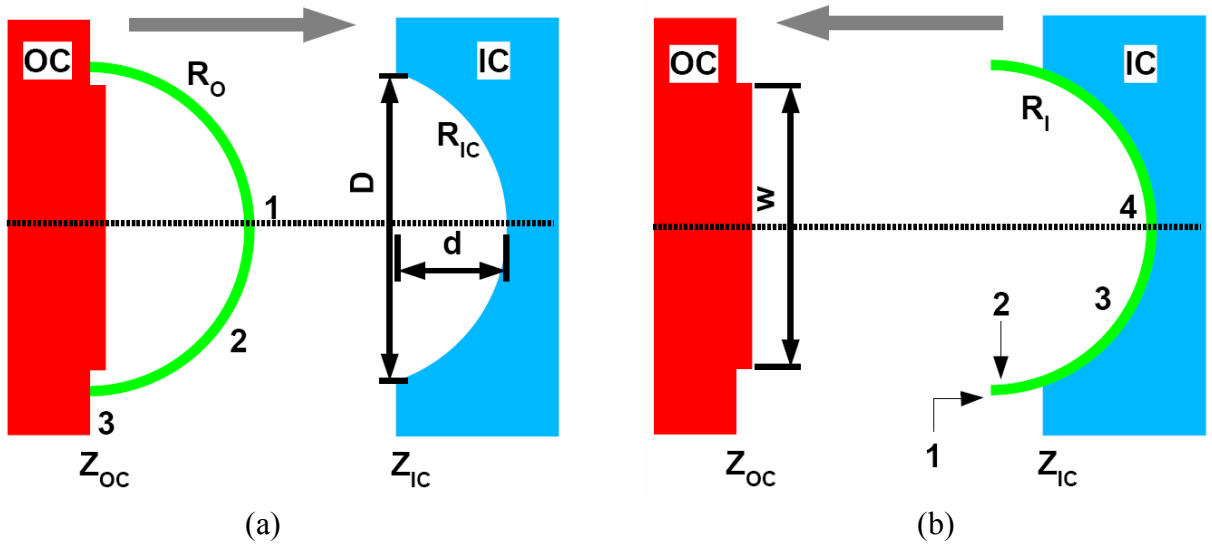

Figure 1. Hemishell transfer. (a) IC to OC transfer and (b) OC to IC transfer.

8.2 PROBE SELECTION

To automatically transfer of a shell from one fixture to another, a sensor is needed to probe the position of the shell with respect to the coordinate system of the machine. The strictest requirement for the transfer and alignment system is that after a hemishell is repositioned on the OC fixture the runout must be no greater than 5 µm.

Several types of probes were considered including capacitance gauges, LVDTs and kinematic touch probes. Capacitance gauges and LVDTs have the necessary accuracy and range of travel, but typically have only one axis of measurement. Since both concave and convex shell surfaces need to be measured either the probe would have to be re-positioned (i.e., rotated 180°) or multiple probes would be required. Custom probe geometries or probe clusters could be used, but at considerable expense. Although continuous analog output from an LVDT or capacitance gauge is ideal for runout measurement, to measure radius of curvature and locate the hemishell

the probe must be moved. Thus the accuracy of the measurement is dependent on the metrology frame of the machine and registration of the probe in the machine coordinate system.

For these reasons a touch probe was selected for this project. Demonstration experiments at the PEC will use a Renishaw TP6 probe (Figure 1) that will be borrowed from the Brown and Sharpe CMM at the Center. This probe is adjustable around a pivot bolt and has a 21 mm gauge length. Since all measurements will be made in the same plane, pretravel variation with angle of contact (i.e., lobing) is not an issue for this application. The probe will be mounted, aligned and calibrated on the ASG 2500 diamond turning machine before the transfer experiments to assess its repeatability and to obtain a map of the virtual probe shape in the measurement plane.

Figure 2. Renishaw TP6 CMM Probe.

8.3 ERROR ASSESSMENT OF SYSTEM PERFORMANCE

For the Renishaw TP6 probe the uncertainty of the measurements needed for the automated shell transfer were evaluated. The measurement uncertainty is a combination of setup errors and probe errors. The following assumptions were made:

1. Machine errors are minimal; that is, the hemishell is centered with the spindle and is round.
2. Machine components on are aligned; that is, the IC and OC chuck spindle axes are collinear.

If these errors are significant, the parts cannot be machined to specification. These assumptions leave only two error sources: probe errors and uncertainty in the alignment of the probe. These errors must be characterized and their relative magnitudes determined. Techniques for minimizing the impact of the identified errors or mapping them through calibration with a known artifact can then be evaluated. Application of the combination of uncertainties for a particular measurement bounds the worst case error.

While most of the probe errors are repeatable and can thus be calibrated and removed from the measurements, the overall repeatability error cannot be avoided. Hence, this repeatability error and the resultant alignment errors must be considered in the measurements. In the case of the Renishaw TP6 probe, the repeatability value given by Renishaw is ±0.35 µm. Adding this to the

expected alignment errors yields uncertainties in the X, Y, and Z directions of 0.63 μm, 3.6 μm and 0.63 μm respectively as shown in Table 1 and discussed in detail in [1].

Table 1. Summary of measurement error uncertainties (μm)

Contributor	X error	Y error	Z error
Probe Ball Geometry	0.125	0.125	0.125
Hertzian Deflection	0.13	0.13	0.13
Stylus Deflection[1]	0.35	0.35	0.35
Repeatability	0.35	0.35	0.35
Probe Setup	0.35	0.35	0.35
Probe Alignment	0.0013	3.6	0
Total	**0.63**	**3.6**	**0.63**

8.4 DATA ANALYSIS ALGORITHMS

Probe data will be used to determine the size and location of a machined hemishell prior to transfer between spindles and to reposition a hemishell after transfer to an OC machining fixture as shown in Figure 1. For both part transfer scenarios, a simple algorithm will calculate the part to fixture clearance at the axial separation required for a successful vacuum transfer. A go/no-go decision will be made based upon the part and receiving fixture radii and clearance at the transfer location. In the case of an affirmative decision (i.e., no interference between the part and receiving fixture), an axial motion command can be initiated on the machine tool controller and displayed on the operator console. Otherwise an error message will be displayed indicating nature of the problem.

To reposition a hemishell on an OC machining fixture, the magnitude and angular orientation of part must be calculated. Two methods of calculating shell runout are given in [1]. Both are straightforward, however one gives a more accurate answer at the expense of a more complex calculation[2]. The second algorithm requires more data points and gives an approximate answer, but may be simpler to implement on the machine controller.

8.4.1 RUNOUT CALCULATION USING RADII DATA

When measuring a rotating part that is round but de-centered on the spindle, probe deflections are described by the general polar equation of a circle. In Equation 1, R is the part radius, $(d_0,$

[1] Can be removed from measurement data after calibration.

[2] The radius and center of a circle are uniquely determined from any three points on its circumference.

φ_0) are the center coordinates of the part, φ is a spindle rotation angle and d is the probe deflection (distance to the origin) at that angle.

$$R^2 = d^2 - 2dd_0\cos(\varphi - \varphi_0) + d_0^2 \tag{1}$$

Without loss of generality let $\varphi_0 = 0$. Rearranging Equation 1 gives an expression for expected probe deflections as a function of rotation angle for a part with a maximum runout of d_0.

$$d = d_0\cos\varphi + \sqrt{R^2 - d_0^2\sin^2\varphi} \tag{2}$$

Clearly when $\varphi = 0$, Equation 2 is at a maximum and gives a value for d of $R + d_0$. Similarly, the minimum value, $R - d_0$, occurs at $\varphi = \pi$. Thus the range of probe deflections is exactly twice the runout. So an estimate of the runout can be obtained by selecting the points of maximum and minimum deflection and performing the simple calculation shown in Equation 3. The accuracy of the estimate increases with the number of data points.

$$d_0 = \frac{1}{2}\left[\max(r_j) - \min(r_j)\right] \quad \forall i \le N \tag{3}$$

This method of estimating runout is equivalent to nearest-neighbor interpolation of Equation 2. For the maximum expected runout value of 2.54 mm the uncertainty in finding the true extreme values for a given number of evenly distributed data values is the same as the interpolation error. To achieve uncertainty less than 5 μm in this calculation the value of N should be at least 37 and the data should be evenly distributed around the part. Figure 3 shows a worst case simulated runout measurement (Equation 2) with a 76.2 mm radius circular part for a range of values for N and runout magnitudes up to the expected maximum. The largest estimation error occurs when the phase of the runout extrema with respect to the sampled data points is one-half of the angular point separation, that is any integer multiple of π/N.

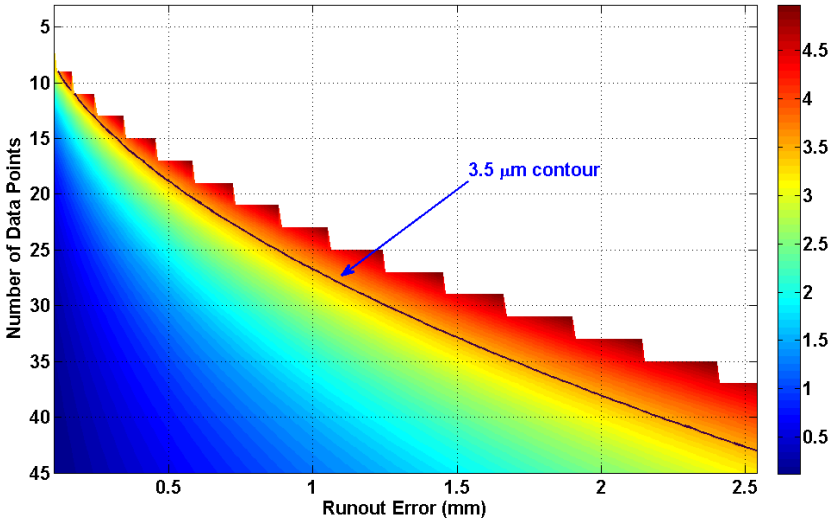

Figure 3. Runout error measurement simulation.

The uncertainty in the value of a single measurement is ±0.63 μm (see Table 1). Since only the largest and smallest values are used in Equation 3, the number of points must be selected so that the sampling error is below 3.74 μm. This sampling always under-estimates the runout for an odd number of data points taken at equal angular spacing (i.e., one or both of the peak and the valley in the true runout motion will always be missed). The smallest value of N that meets the criteria is 43, for which the sampling error is 3.50 μm. The worst case runout calculation uncertainty using this algorithm with $N = 43$ is $3.50 + 2(0.63) = 4.76$ μm.

8.5 CONCLUSIONS AND FUTURE WORK

Phase 1 of the project has been completed. A sensor has been selected and data analysis algorithms developed to ensure that the calculation of shell location, shape and runout will be within the specified tolerances. A system error assessment has been conducted and the expected performance of the runout calculation simulated. The layout of components for demonstration of both transfer operations and the runout measurement using equipment at the PEC (i.e., the ASG 2500 diamond turning machine) has begun. The demonstration parts (IC, OC vacuum chucks and 6 inch diameter hemishell) have been rough machined and are shown in Figure 4.

Figure 4. IC (left) and OC (right) vacuum chucks and unfinished hemishell (center).

REFERENCES

1. Dow, T., K. Garrard and A. Sohn. Automatic Handling Technology for Hemispherical Shells, Interim Report – Task I, Sensor Selection. Precision Engineering Center, North Carolina State University (2007).